water

MDPI

Article

Spatiotemporal Analysis of Water Quality and Optical Changes Induced by Contaminants in Lake Chinchaycocha Using Sentinel-2 and in Situ Data

Emerson Espinoza [1], Analy Baltodano [2] and Norvin Requena [1,*]

[1] Grupo de Investigación en Residuos para el Desarrollo Sostenible (GIRDS), Facultad de Ingeniería Ambiental, Universidad Nacional de Ingenieria, Av. Tupac Amaru 210, Rimac, Lima 1333, Peru; emerson.espinoza.b@uni.pe

[2] Department of Water and Climate, Vrije Universiteit Brussel, 1050 Brussels, Belgium; baltodano.martinez.analy@vub.be

* Correspondence: nrequenas@uni.edu.pe

Abstract

Lake Chinchaycocha, Peru's second-largest high-altitude lake and a Ramsar-designated wetland of international importance, is increasingly threatened by anthropogenic pollution and hydroclimatic shifts. This study integrates Sentinel-2 multispectral imagery with in situ water quality data from Peru's National Water Observatory to assess spatiotemporal dynamics in 31 physicochemical parameters between 2018 and 2024. We evaluated 40 empirical algorithms developed globally for Sentinel-2 and tested their transferability to this ultraoligotrophic Andean system. The results revealed limited predictive accuracy, underscoring the need for localized calibration. Subsequently, we developed and validated site-specific models for ammoniacal nitrogen, electrical conductivity, major ions, and trace metals, achieving high predictive performance during the rainy season (R^2 up to 0.95). Notably, the study identifies consistent seasonal correlations—such as between total copper and ammoniacal nitrogen—and strong spectral responses in Band 1, linked to runoff dynamics. These findings highlight the potential of combining public monitoring data with remote sensing to enable scalable, cost-effective assessment of water quality in optically complex, high-Andean lakes. The study provides a replicable framework for integrating national datasets into operational monitoring and environmental policy.

Keywords: Sentinel-2 MSI; remote sensing; water quality modeling; empirical algorithms; high-altitude Andean lakes; ultraoligotrophic ecosystems; national water observatory; seasonal reflectance dynamics

check for updates

Academic Editors: Rongkui Su and Yiting Luo

Received: 24 June 2025
Revised: 13 July 2025
Accepted: 14 July 2025
Published: 23 July 2025

Citation: Espinoza, E.; Baltodano, A.; Requena, N. Spatiotemporal Analysis of Water Quality and Optical Changes Induced by Contaminants in Lake Chinchaycocha Using Sentinel-2 and in Situ Data. *Water* **2025**, *17*, 2195. https://doi.org/10.3390/w17152195

Copyright: © 2025 by the authors. Licensee MDPI, Basel, Switzerland. This article is an open access article distributed under the terms and conditions of the Creative Commons Attribution (CC BY) license (https://creativecommons.org/licenses/by/4.0/).

1. Introduction

The global deterioration of freshwater quality is a critical environmental issue with far-reaching implications for aquatic ecosystem structure, function, and resilience [1]. This decline is driven by multiple anthropogenic stressors, including industrial discharges, agricultural runoff, and untreated urban effluents [2]. In this context, systematic water quality monitoring is essential to detect temporal changes in chemical composition and support evidence-based environmental management [3].

Remote sensing has emerged as a key technology for large-scale assessment of water quality, offering the ability to detect spatiotemporal patterns with high resolution and frequent revisit times. It provides a complementary approach to conventional in situ

monitoring, especially in remote or logistically challenging regions [4,5]. However, current applications are predominantly limited to optically active water constituents such as chlorophyll-a (Chl-a), colored dissolved organic matter (CDOM), turbidity, and total suspended solids (TSS), all of which have well-defined spectral responses. Conversely, parameters such as potential of hydrogen (pH), total nitrogen (TN), and total phosphorus (TP) remain difficult to quantify due to weak optical signatures and elevated signal-to-noise ratios in satellite reflectance data [6].

Despite these challenges, integrating remote sensing observations with predictive models—including empirical, semi-analytical, or machine learning frameworks—has enabled the anticipation of water quality dynamics and informed decision-making processes in hydrological management [7]. Nevertheless, remote sensing remains susceptible to several constraints. These include interference from cloud cover, limited spatial–temporal availability of cloud-free imagery [8], and the indispensable requirement for extensive ground-based measurements to support model calibration and validation. Moreover, empirical models calibrated under specific conditions frequently show poor transferability when applied across different geographic or ecological settings, which compromises their generalizability and predictive robustness [9].

To enhance model applicability, there is a growing need to assemble extensive multitemporal datasets that integrate both satellite-derived and field-based observations [10]. In particular, the use of harmonized in situ monitoring databases containing physicochemical parameters such as Chl-a, TSS, and Secchi depth (SDD) is critical for developing context-sensitive and scalable models of water quality.

At the international level, datasets such as the Global Lakes Observatory for Radiance and In Situ Assessment (GLORIA) have significantly advanced the performance of predictive water quality models. GLORIA comprises over 7000 georeferenced and radiometrically corrected hyperspectral measurements, paired with key indicators such as Chl-a, TSS, and SDD, covering diverse lake typologies across multiple continents [10,11]. In Asia, China's Zhejiang Ecological Environment Monitoring Center has established an automated network of 311 stations that, between 2019 and 2023, collected near-real-time data on Chemical Oxygen Demand (permanganate method; COD-Mn), TN, TP, ammoniacal nitrogen (NH_3-N), and turbidity—offering a robust basis for remote sensing validation [12]. Similarly, in Europe, the German Federal Environment Agency compiled detailed records on turbidity, Chl-a, and SDD across 112 water bodies as part of the Water Framework Directive (WFD) implementation between 2016 and 2020 [9].

In Latin America, national programs have made significant strides toward enhancing water quality databases. The National Water Quality Monitoring Network (RNMCA) in Mexico, managed by the National Water Commission (Comisión Nacional del Agua, CONAGUA), compiled daily physicochemical measurements between 2012 and 2018 as part of a national strategy for surface water governance. These records are particularly advantageous for remote sensing studies, as they provide temporally aligned datasets for model calibration. Recent research using RNMCA data and Sentinel-2 imagery has demonstrated strong correlations for parameters such as chlorophyll-a and turbidity in various inland water bodies [13].

In the Peruvian context, the National Water Authority (Autoridad Nacional del Agua, ANA) has maintained a comprehensive water quality monitoring program since 2010 under the Water Resources Law. Unlike automated monitoring stations, these field-based measurements adhere to strict sampling protocols, employ accredited analytical methods, and are processed in specialized laboratories. With over 3100 monitoring points nationwide, including 248 in trans-boundary basins, ANA generates annual datasets updated through analyses conducted by certified laboratories [14]. Despite their scope, these records remain

largely underutilized in satellite-based water quality research, representing an untapped opportunity to strengthen model calibration and support regional adaptation strategies.

While countries like China and Germany have effectively leveraged publicly available governmental datasets for empirical model development, many aquatic systems—particularly those with complex ecological dynamics—require localized databases tailored to specific environmental conditions. In Peru, ANA's extensive archive of historical observations holds significant potential to enhance remote sensing applications and improve model precision.

Maximizing the utility of national environmental datasets requires not only technical integration but also institutional coordination. Embedding scientific methods into policy frameworks and aligning data collection efforts across agencies are essential for ensuring the long-term effectiveness of water quality monitoring technologies [15].

In this context, the present study proposes a methodological framework that integrates in situ data from Peru's National Water Observatory (ONRH) into remote sensing-based models. Although underutilized in most remote sensing applications in Peru, these institutional datasets offer considerable potential for developing robust, region-specific predictions [9,13]. Furthermore, aligning field sampling campaigns with satellite overpasses enhances data consistency and supports more informed, timely, and effective decision-making in environmental management.

Considering these needs and opportunities, the objective of this study is to develop and evaluate predictive models for water quality in Lake Chinchaycocha using Sentinel-2 imagery combined with in situ data. The research begins with a review of existing empirical models and their applicability to high-altitude Andean ecosystems. It then explores the statistical relationships between spectral bands and physicochemical parameters, incorporating seasonal variability. Based on this analysis, a set of locally calibrated predictive models is generated and validated using performance metrics such as the coefficient of determination (R^2), root mean square error (RMSE), and mean absolute percentage error (MAPE). Finally, the study highlights the potential for broader integration of governmental datasets into operational remote sensing workflows aimed at improving water quality management across similar regions.

2. Materials and Methods

2.1. Study Area Description

Lake Chinchaycocha, also known as Junin, is situated in the Junín region of the central Peruvian Andes at an elevation of 4100 m above sea level. It is the country's second-largest lake and forms part of the Junín National Reserve, a protected area recognized in 1997 as a Wetland of International Importance under the Ramsar Convention due to its global ecological significance [16]. The lake spans approximately 470 km^2, with an average depth between 8 and 12 m in its central region [17].

The climate in this high Andean puna ecosystem is characterized by sharp diurnal temperature fluctuations (6 °C to 27 °C) and variable relative humidity (30–79%). Solar irradiance also shows considerable variation, ranging from 0.36 to 239 mW/m^2 [18]. The lake is part of the Upper Mantaro River Basin and experiences marked seasonality, with intense precipitation from October to March (rainy season) and minimal rainfall, typically below 20 mm per month, between May and August (dry season) [19].

Hydrologically, Chinchaycocha is fed by 12 primary rivers and 20 smaller streams, creating a dynamic and complex aquatic system [20]. It supports the highest avian diversity among Peru's high-Andean wetlands, hosting around 70 bird species throughout the year [21]. The surrounding landscape comprises wetlands, reed beds, and grasslands that serve as important carbon sinks, contributing to regional climate regulation [22].

However, the lake faces critical ecological threats. Endemic and endangered species such as the Junín giant frog (*Telmatobius macrostomus*), the Junín grebe (*Podiceps taczanowskii*) and the black rail (*Laterallus tuerosii*) are under pressure due to ongoing environmental degradation [17,18,23]. Historically, the discharge of mining waste from tributaries has led to the accumulation of heavy metals and toxic substances, compromising both ecosystem health and nearby human communities [24]. Additionally, pressures from livestock farming, agriculture, and untreated wastewater discharges have exacerbated the degradation of water quality and aquatic habitats [25].

The geographic context of Lake Chinchaycocha, including the spatial distribution of monitoring stations and relevant environmental features, is shown in Figure 1. This includes geospatial layers such as ecosystem classifications provided by the Ministry of the Environment (Ministerio del Ambiente, MINAM) [26], agricultural land-use maps from the Ministry of Agrarian Development and Irrigation (Ministerio de Desarrollo Agrario y Riego, MIDAGRI) [27], pollution-source inventories from the National Water Authority (Autoridad Nacional del Agua, ANA) [14], the boundaries of protected areas managed by the National Service of Natural Protected Areas (Servicio Nacional de Áreas Naturales Protegidas por el Estado, SERNANP) [28], and the Initial Inventory of Mining Environmental Liabilities compiled by the Ministry of Energy and Mines (Ministerio de Energía y Minas, MINEM) [29].

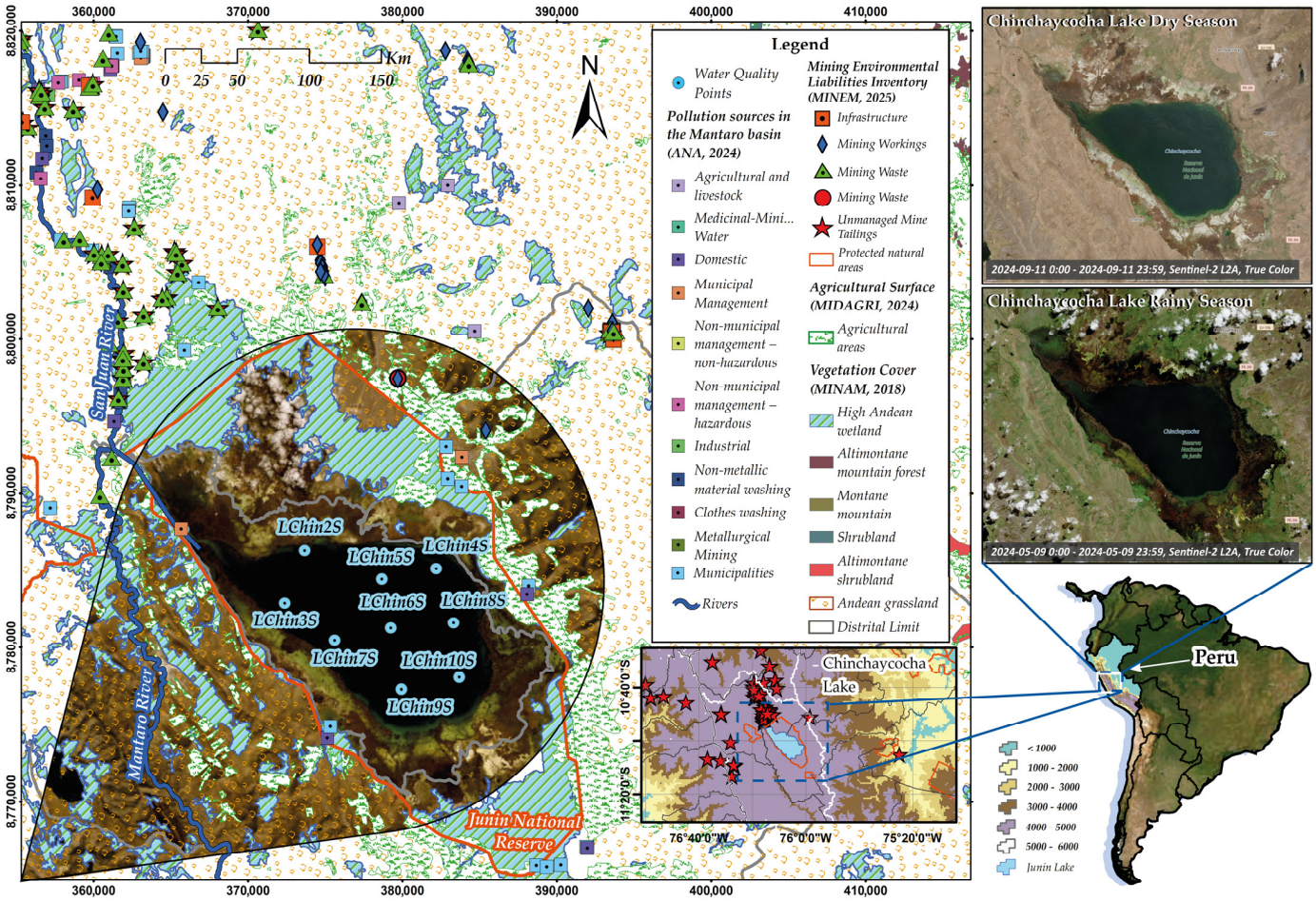

Figure 1. Geographical location of Lake Chinchaycocha and surrounding features.

As shown in Figure 1, the northern sector of Lake Chinchaycocha is characterized by a high density of mining environmental liabilities and active mining operations, particularly along the banks of the San Juan River. This area is also surrounded by extensive agricultural

zones, creating potential synergistic impacts on water quality due to the combined effects of industrial discharges and agrochemical runoff.

2.2. Data of Water Quality Parameters

The Observatorio Nacional de Recursos Hídricos (ONRH), managed by the Autoridad Nacional del Agua (ANA) under Peru's Ministry of Agrarian Development and Irrigation (Ministerio de Desarrollo Agrario y Riego), is responsible for integrating and managing hydrological and water quality data nationwide [14]. This information is available online through the official portal: https://snirh.ana.gob.pe/onrh/ (accessed on 13 January 2025).

For this study, ANA provided laboratory analysis reports, equipment calibration records, and participatory monitoring data for the Mantaro River Basin and Lake Chinchaycocha. All data were consolidated into a structured alphanumeric database.

To ensure temporal compatibility with satellite acquisitions, only sampling dates that coincided with Sentinel-2 overpasses were selected, allowing a maximum offset of three days. This threshold was established based on prior studies [7,30–33], which demonstrate that ±3-day windows minimize bio-optical variability while providing sufficient matchups for model calibration.

Water quality monitoring campaigns were conducted in May and September 2018, June and September 2019, June and October 2021, and May and October 2022. Ten strategically distributed sampling points were selected across Lake Chinchaycocha, following the design established by ANA. Monitoring point LChin1S was excluded due to spatial resolution constraints. As recommended by Hestir et al. [34], priority was given to stations located in water bodies with a width exceeding the maximum Sentinel-2 spatial resolution (60 m) to minimize spectral mixing effects with surrounding vegetation. Additionally, the October 2024 Sentinel-2 image, included in the ANA dataset, was reserved exclusively for model validation during the dry season to ensure independence from the calibration dataset.

The analyzed physicochemical and inorganic parameters are listed in Table 1, along with their corresponding Peruvian Environmental Water Quality Standards (Supreme Decree N° 004-2017-MINAM, Category 4: Conservation of the aquatic environment) [35].

Table 1. Water Quality Parameters for Chinchaycocha Lake during Total, Dry, and Rainy Seasons. (N: Number of Samples; N*: Number of Samples did not exceed the limit of quantification (LOQ); Avg: Average Value; SD: Standard Deviation; Min: Minimum Value; Max: Maximum Value).

Parameters	Unit	Water Quality Standard	Total				Dry Season			Rainy Season		
			N	N*	Avg	SD	N	Min	Max	N	Min	Max
Physicochemical												
Field parameters												
pH	--	6.5–9.0	57	0	8.71	0.19	27	8.408	9.174	30	7.962	8.70
Temperature	°C	Δ3	57	0	12.51	3.49	27	11.59	16.91	30	3.988	11.05
Conductivity	µS/cm	1000	57	0	275.46	9.67	27	254	290.7	30	256.2	276.26
Dissolved Oxygen	mg O_2/L	≥5	57	0	7.786	0.85	27	6.246	10.064	30	6.451	7.70
Laboratory parameters												
Chlorophyll-a	mg/L	0.008	51	51	--	--	21	<0.003	<0.0041	30	<0.003	<0.0041
Total Suspended Solids (TSS)	mg/L	≤ 25	57	56	4	4	27	<2	<3	30	<2	4

Table 1. *Cont.*

Parameters	Unit	Water Quality Standard	Total				Dry Season			Rainy Season		
			N	N*	Avg	SD	N	Min	Max	N	Min	Max
Oils and Greases	mg/L	5	57	57	--	--	27	<0.4	<1	30	<0.4	<1
Total Nitrogen	mg N/L	0.315	57	3	0.587	0.20	27	0.13	1.05	30	<0.1	0.892
Ammoniacal Nitrogen	mg NH_3-N/L	--	39	1	0.122	0.05	18	<0.006	0.186	21	0.048	0.214
Nitrates	mg NO_3^-/L	13	57	25	0.180	0.06	27	<0.009	0.509	30	<0.062	0.207
Nitrates (as N)	mg NO_3-N/L	--	30	1	0.040	0.006	12	<0.002	0.051	18	0.034	0.047
Chemical Oxygen Demand	mg O_2/L	--	9	0	11	4.83	-	-	-	9	4	19
Chlorides	mg Cl^-/L	--	21	0	4.918	0.64	12	5.02	6.687	9	3.998	4.514
Total Phosphorus	mg P/L	0.035	57	49	0.064	0.03	27	<0.01	0.099	30	<0.007	0.01
Inorganic												
Total Aluminum	mg/L	--	57	48	0.0093	0.0073	27	<0.002	0.011	30	<0.002	0.027
Total Antimony	mg/L	0.64	57	20	0.0006	0.0002	27	<0.00013	0.0008	30	<0.00004	0.0009
Total Arsenic	mg/L	0.15	57	1	0.0034	0.0008	27	<0.0001	0.0057	30	0.0012	0.00446
Total Barium	mg/L	0.7	57	0	0.0342	0.0053	27	0.0258	0.0415	30	0.0193	0.0406
Total Boron	mg/L	--	57	25	0.0123	0.0098	27	<0.006	0.057	30	<0.002	0.011
Total Calcium	mg/L	--	57	0	36.123	5.4328	27	24.671	42.87	30	27.308	45.9
Total Copper	mg/L	0.1	57	3	0.002	0.0006	27	<0.00009	0.00311	30	<0.00009	0.00353
Total Strontium	mg/L	--	57	0	0.2044	0.0174	27	0.1831	0.2389	30	0.1521	0.2269
Total Iron	mg/L	--	57	28	0.0298	0.0753	27	<0.0004	0.415	30	<0.0004	0.0691
Total Lithium	mg/L	--	57	0	0.0092	0.0020	27	0.0076	0.0148	30	0.0044	0.0111
Total Magnesium	mg/L	--	57	0	9.4673	0.9873	27	8.257	12.282	30	8.206	11.084
Total Manganese	mg/L	--	57	0	0.037	0.0181	27	0.0082	0.0784	30	0.01391	0.10913
Total Molybdenum	mg/L	--	57	9	0.0004	0.0001	27	<0.00006	0.00097	30	<0.00002	0.00063
Total Potassium	mg/L	--	57	0	1.192	0.2069	27	1.12	1.62	30	0.6	1.33
Total Silicon	mg/L	--	48	0	2.220	0.5092	27	1.5	2.906	21	1.17	3.2
Total Sodium	mg/L	--	57	0	6.312	0.7838	27	5.517	8.617	30	5.376	6.757
Total Zinc	mg/L	0.12	57	4	0.026	0.0202	27	<0.008	0.1177	30	<0.01	0.0599

Note: Biochemical Oxygen Demand (BOD_5), Phenols, and Free Cyanide concentrations remained below the analytical method detection limits (MDLs) across all sampling periods, indicating values below the quantifiable range of the laboratory assays. pH is a dimensionless parameter.

2.3. Satellite Image Data and Reflectance Extraction

Twelve atmospherically corrected Sentinel-2 Level-2A surface reflectance images were acquired from the Copernicus Open Access Hub (https://dataspace.copernicus.eu/explore-data (accessed on 13 January 2025)). These products provide high spatial and spectral resolution, making them suitable for assessing water quality in inland aquatic systems. The spectral characteristics of each band, including central wavelengths and

spatial resolutions, follow the Sentinel-2 MSI technical specifications [36] and are detailed in Appendix A Table A1.

Surface reflectance values were extracted in QGIS and precisely georeferenced to match in situ sampling locations. This alignment ensured accurate spectral data retrieval and facilitated robust comparisons with ground-based measurements.

Table 2 presents the acquisition dates of the selected images and their temporal proximity to corresponding in situ measurements. All images met the ±3-day window criterion to ensure temporal consistency between satellite overpasses and field sampling.

Table 2. Acquisition dates of Sentinel-2 images and temporal offset relative to field campaigns.

Image Date	Season	Image ID	Δ Days (Satellite–Field)
26 October 2024	Dry	01 *	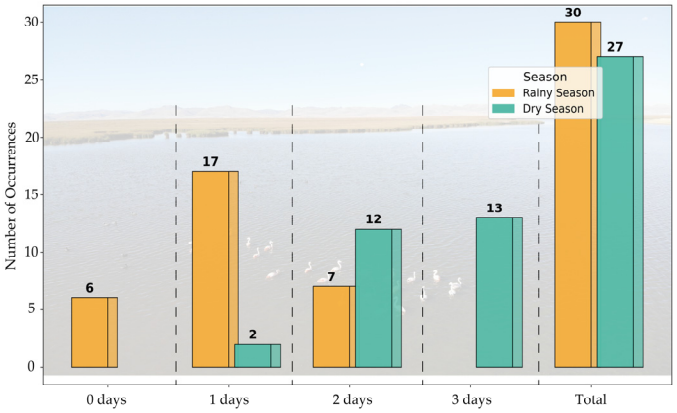
22 October 2022	Dry	02	
5 May 2022	Rainy	03	
12 October 2021	Dry	04	
9 June 2021	Rainy	05	
8 September 2019	Dry	06	
25 June 2019	Rainy	07	
8 September 2018	Dry	08	
21 May 2018	Rainy	09	

Note: * Image 01 (October 2024) was reserved exclusively for dry-season model validation and excluded from calibration procedures.

2.4. Phase 1: Evaluation of Empirical Formulas

Table 3 summarizes a selection of empirical algorithms previously developed for estimating water quality parameters using Sentinel-2 spectral data. These models, drawn from diverse geographical contexts, exhibit varying degrees of correlation (R^2) with field-based observations. To assess their applicability in high-altitude Andean environments, each algorithm was independently tested against local in situ data. Priority was given to those models with the strongest reported correlations and those that excluded Sentinel-2 Band 10 due to its limited relevance in water quality analysis.

Table 3. Empirical algorithms using Sentinel-2.

Adjusted Algorithm	Error	Code	Study Area	Source	Units
Physicochemical parameters					
Potential of Hydrogen (pH)					
$\mathbf{4.925 - 0.03739\left(\frac{B6}{B4-B8}\right) + 2.478(B7/B6)}$	R^2 = 0.842, RMSE = 0.15	PH-01	Bajo Sinú Wetlands, Colombia	Bejarano et al. [37]	--
$\mathbf{12.2621 - 246.4698(B1) + 29.4987(B3) + 300.0727(B6) - 140.2648(B8)}$	r^2 = 0.89, RMSE = 0.04	PH-02	Tres Marias Reservoir, Brazil	Pizani et al. [38]	--
$\mathbf{-87.11(B5) + 16.928}$	R^2 = 0.6	PH-03	Setumo Dam reservoir, South Africa	Ndou [39]	--

Table 3. *Cont.*

Adjusted Algorithm	Error	Code	Study Area	Source	Units
Conductivity (EC)					
$\mathbf{18.707(NDSI) + 23.343}$	R^2 = 0.718	EC-01	Bangweulu Wetland, Zambia	Chundu et al. [40]	µS/cm
$\mathbf{-0.778(B2) + 0.849(B5) - 0.3973(B06) + 1152.8}$	R^2 = 0.69 RMSE = 97	EC-02	Aras River Basin, Turkey and Neighbors	Fouladi et. al. [7]	µS/cm
$\mathbf{580.2 - 212.8(B5/B3) - 62.7(B7/B8)}$	R^2 = 0.735, RMSE = 8.54	EC-03	Bajo Sinú Wetlands, Colombia	Bejarano et al. [37]	µS/cm
$\mathbf{20(B4) + 0.0393}$	R^2 = 0.7	EC-04	Setumo Dam reservoir, South Africa	Ndou [39]	dS/m
Dissolved Oxygen (DO)					
$\mathbf{0.00075(B2) + 0.00989(B3) - 7.09}$	R^2 = 0.56 RMSE = 0.65	DO-01	Hassan Addakhil Reservoir, Morocco	El Ouali et al. [41]	mg O_2/L
$\mathbf{-1.687 + 13.65(B5/(B4 + B8A)) - 0.3714(B4/(B7 - B8))}$	R^2 = 0.778 RMSE = 0.60	DO-02	Bajo Sinú Wetlands, Colombia	Bejarano et al. [37]	mg O_2/L
$\mathbf{9.2505 - 171.0251(B2) + 236.9708(B4) + 76.8288(B6) - 150.7815(B11)}$	r^2 = 0.85 RMSE = 0.07	DO-03	Tres Marias Reservoir, Brazil	Pizani et al. [38]	mg O_2/L
$\mathbf{22.228 + 46.834x + 45.3098x^2 + 12.8509x^3}$, $\mathbf{x = (B3 - B5 - B11/B12)}$	R^2 = 0.728 RMSE = 1.272	DO-04	Guangli River, Huaihe River Basin, China	Cao et al. [3]	mg O_2/L
Chlorophyll A (Chl-a)					
$\mathbf{0.0003214(B5) + 0.000378(B6) + 0.0013207(B8) - 0.126}$	R^2 = 0.58 RMSE = 0.07	CHL-01	Hassan Addakhil Reservoir, Morocco	El Ouali et al. [41]	µg/L
$\mathbf{576.51\left(\frac{B7}{B8}\right)^2 - 1126.6\left(\frac{B7}{B8}\right) + 583.14}$	$R^2_{B7/B8}$ = 0.835, NRMSE = 0.14	CHL-02	Burullus Lake, Egypt	Hossen et al. [42]	µg/L
$\mathbf{26.447 - 1672.777(B2) + 266.620(B3) + 1402.560(B4) - 58.610(B5)}$	r^2 = 0.71, RMSE = 0.92	CHL -03	Tres Marias Reservoir, Brazil	Pizani et al. [38]	µg/L
$\mathbf{-0.001(486(NDVI) + 44)}$	---	CHL-04	Manyame Lake, Zimbabwe	Kowe et al. [43]	µg/L
$\mathbf{395763x^2 - 44991x + 1288.2}$, $\mathbf{x = B2 - B11}$	R^2 = 0.701 RMSE = 12.84	CHL-05	Chebara Dam reservoir, Kenia	Ouma et al. [44]	µg/L
Chemical Oxygen Demand (COD)					
$\mathbf{218.75 - 4271.43(B2) + 3214.16(B3) - 561.44(B4)}$	R^2 = 0.67	COD-1	Manyame and Dande Rivers, Zimbabwe	Wang et al. [45], Muhoyi et al. [46]	mg/L
Total Nitrogen (TN)					
$\mathbf{\exp(1.10\left(\frac{B4}{B2}\right) - 0.30\left(\frac{B2}{B4}\right) - 3.16(B4) - 0.40)}$	R^2 = 0.78	TN-01	Manyame River and Dande River, Zimbabwe	Torbick et al. [47], Muhoyi et al. [46]	mg N/L
$\mathbf{16.995(B8A)^2 - 0.1979(B8A) + 2.527}$	R^2_{B8A} = 0.619, NRMSE = 0.27	TN-02	Burullus Lake, Egypt	Hossen et al. [42]	µg N/L
$\mathbf{1.047532 - 54.928(B2) - 46.2947(B3) + 120.8943(B4) - 19.223(B8)}$	r^2 = 0.63	TN-03	Manyame Lake, Zimbabwe	Kapalanga et al. [48] Kowe et al. [43]	mg N/L
$\mathbf{-0.194(B2 \times B8)^2 + 1.962B2 \times B8 - 1.955}$	R^2 = 0.783 RMSE = 0.079	TN-04	Danjiangkou Reservoir, China	Dong et al. [49]	mg N/L
$\mathbf{128.6065(e)^{-1.8090((B3+B8A))/(B2+B12))}}$	R^2 = 0.657	TN-05	Branch River Chenqiao, China	Cao et al. [3]	mg N/L

Table 3. *Cont.*

Adjusted Algorithm	Error	Code	Study Area	Source	Units
Total Phosphorus (TP)					
$\mathbf{exp(2.53 + 1.04(B4) - 0.97(\frac{B4}{B2}) - 1.42(\frac{B2}{B4}))}$	R^2 = 0.63	TP-01	Manyame and Dande Rivers, Zimbabwe	Torbick et al. [47], Muhoyi et al. [46]	mg P/L
$\mathbf{36.201(\frac{B8}{B3})^2 + 92.078(\frac{B8}{B3}) + 230.74}$	$R^2_{B8/B3}$ = 0.733, NRMSE = 0.16	TP-02	Burullus Lake, Egypt	Hossen et al. [42]	µg P/L
$\mathbf{0.89(B4) - 0.093}$	R^2 = 0.61, p = 0.023	TP-03	Weihe River, China	Liu et al. [50]	mg P/L
$\mathbf{165.9(B5/B3)^3 - 466.7(B5/B3)^2 + 434.3(B5/B3) - 133.4}$	R^2 = 0.8359 RMSE = 0.0568	TP-04	Huaihe River Basin, China	Shi et al. [51]	mg P/L
Nitrates (N)					
$\mathbf{0.003099(B1) - 0.000944(B3) + 0.0010509(B4) - 1.81}$	R^2 = 0.62 RMSE = 0.16	N-01	Hassan Addakhil Reservoir, Morocco	El Ouali et al. [41]	mg NO_3-N/L
$\mathbf{0.095(B1) - 0.014(B2) - 0.0262(B3) - 0.0126(B9) - 66.442}$	R^2 = 0.671 RMSE = 0.618	N-02	The Bin El Ouidane Reservoir, Azilal, Morocco	Ismail et al. [52]	mg NO_3-N/L
Ammoniacal Nitrogen (NH_3–N)					
$\mathbf{3.333(\frac{B7}{B1})^2 - 9.328(\frac{B7}{B1}) + 6.56}$	R^2 = 0.9036 RMSE = 0.0397	AN-01	Huaihe River Basin, China	Shi et al. [51]	mg NH_3-N/L
$\mathbf{0.474\frac{B3}{B2} + 0.276}$	R^2 = 0.739 RMSE = 0.0107	AN-02	Danjiangkou Reservoir, China	Dong et al. [49]	mg NH_3-N/L
$\mathbf{NH_4^+N = 11.17(B4) - 0.46}$	R^2 = 0.62 p = 0.020	AN-03	Weihe River, China	Liu et al. [50]	mg NH_3-N/L
$\mathbf{0.0585}(e)^{\mathbf{-0.8332(B4/(B5-B12))}}$	R^2 = 0.7390	AN-04	Branch River Chenqiao, China	Cao et al. [3]	mg NH_3-N/L
Total Suspended Solids (TSS)					
$\mathbf{4.83 - 10.09(B3) - 0.37(B4) - 3.32(\frac{B2}{B3})}$	R^2 = 0.71	TSS-01	Manyame and Dande Rivers, Zimbabwe	Song et al. [53], Muhoyi et al. [46]	mg/L
$\mathbf{4.6689}(exp)^{\mathbf{10.609(B3)}}$	R^2 = 0.615 RMSE = 7.34	TSS-02	Bodri River Estuary, Indonesia	Maslukah et al. [54]	mg/L
$\mathbf{93011}x^2 - \mathbf{82773}x + \mathbf{18442}, x = (B4 + (B8/B4))/2$	R^2 = 0.61 RMSE = 8.384	TSS-03	Chebara Dam reservoir, Kenia	Ouma et al. [44]	mg/L
$\mathbf{1956.2(B4) - 50.056}$	R^2 = 0.65 RMSE = 6.27	TSS-04	Banjir Kanal Barat River, Semarang, Indonesia	Wirasatriya et al. [55]	mg/L
Inorganic parameters					
$\mathbf{Na^+ = 7.740(NDSI) + 0.855}$	R^2 = 0.664	NA-01	Bangweulu Wetland, Zambia	Chundu et al. [40]	mg/L **
$\mathbf{Mg^{2+} = -0.00258(B2) + 0.00223(B5) - 0.0008(B7) + 4.0233}$	R^2 = 0.68	MG-01	Aras River Basin, Turkey and Neighbors	Fouladi et al. [7]	mEq/L *
$\mathbf{Na^+ = -0.0033(B2) + 0.0033(B5) - 0.0016(B12) + 3.395}$	R^2 = 0.67	NA-02	Aras River Basin, Turkey and Neighbors	Fouladi et al. [7]	mEq/L *
$\mathbf{Cl^- = -0.0035(B2) + 0.0037(B5) - 0.00205(B12) + 3.8242}$	R^2 = 0.71	CL-01	Aras River Basin, Turkey and Neighbors	Fouladi et al. [7]	mEq/L *

Notes: * Values in mEq/L are converted to mg/L by multiplying by Mg^{2+} (12.1525), Na^+ (23), Cl^- (35.453). ** We use the band combination used by the author.

2.5. Phase 2: Development of New Equations for Lake Chinchaycocha

2.5.1. Regression Models for Water Quality Estimation

This phase focused on developing site-specific empirical models to estimate water quality parameters based on Sentinel-2 surface reflectance data, using in situ measurements as reference values. The general form of the models is given by:

$$Y = F(X) \tag{1}$$

where Y represents the target water quality parameter and X represents one or more spectral bands predictors. Based on previous literature and reflectance behavior in aquatic environments [3,56], the following functional forms were evaluated:

$$Linear \ : \ y \ = \ a \ + \ bx \tag{2}$$

$$Exponential \ : \ y = ae^{bx} \tag{3}$$

$$Logarithmic \ : \ y = a + blnx \tag{4}$$

$$Power \ : \ y = ax^{b} \tag{5}$$

$$Polynomial \ : \ y = a + b_1x + b_2x^2 \ and \ y = a + b_1x + b_2x^2 + b_3x^3 \tag{6}$$

Additionally, Generalized Linear Models (GLMs) were applied to accommodate multiple predictors and nonlinear relationships characteristic of optically complex inland waters [7,57–59]. The general structure of a GLM is expressed as:

$$Y = \ a + b_1X_1 + b_2X_2 + \cdots + b_kX_k \tag{7}$$

All models were evaluated based on their predictive accuracy and statistical robustness using the coefficient of determination (R^2), root mean square error (RMSE), mean absolute percentage error (MAPE), and p-values.

2.5.2. Spectral Band Combinations and Indices

A systematic assessment was conducted using individual spectral bands, mathematical transformations (e.g., ratios, products, differences, and sums), and widely adopted spectral indices relevant to water quality modeling [44,51], see Table 4.

Table 4. Spectral band combinations evaluated.

Combination Type	Formula Example
Single band	$B_{S2A1} = B_{S2Ai}$
Linear band combination	$B_{S2A2} = B_{S2Ai} \ \pm \ B_{S2Aj}$
Band ratios	$B_{2A3} = \frac{B_{S2Ai}}{B_{S2Aj}}$
Mixed band combinations	$B_{2A4} = \frac{B_{S2Ai}}{B_{S2Aj}} \pm B_{S2Ak}$

Note: where i, j, k ∈ {1, 2, . . ., 12, 8A}, corresponding to Sentinel-2A Level-2A surface reflectance bands.

Several established indices were computed to enhance the detection of optically relevant properties. Derived indices used in this study were compiled from Saberioon et al. [60] and Gerardo y de Lima [61], see Table 5.

Table 5. Complementary spectral indices derived from Sentinel-2.

Index	Definition Based on Sentinel 2	Reference
Modified Normalized Difference Water Index ($MNDWI_2$)	$\frac{B3-B12}{B3+B12}$	Xu [62]
Normalized Difference Salinity Index (NDSI)	$\frac{B3-B11}{B3+B11}$	Khan et al. [63] and Guo et al. [64]
Normalized Difference Aquatic Vegetation Index (NDAVI)	$\frac{B8-B2}{B8+B2}$	Villa et al. [65]
Normalized Difference Vegetation Index (NDVI)	$\frac{B8-B4}{B8+B4}$	Tucker C.J. [66]
Green Normalized Difference Vegetation Index (GNDVI)	$\frac{B8-B3}{B8+B3}$	Gitelson & Merzlyak [67]
Normalized Difference Turbidity Index (NDTI)	$\frac{B4-B3}{B4+B3}$	Lacaux et al. [68]
Water Ratio Index 1 (WRI1)	$\frac{B3+B4}{B8+B11}$	Mukherjee & Samuel [69]
Automated Water Extraction Index 1 (AWEI1)	$4(B3-B11)-(0.25(B8)+2.75(B11))$	Feyisa et al. [4]

2.5.3. Construction of Composite Water Quality Indices

To capture hydrochemical gradients, composite indices were derived by summing standardized in situ concentrations (mg L^{-1}) of related parameters (see Table 6):

Table 6. Composite indices derived from in situ data.

Index	Abbrev.	Formula (mg L^{-1})
Sum of major ions	TDS_1	$[Ca^{2+}] + [Sr^{2+}] + [Mg^{2+}] + [K^+] + [Si] + [Na^+]$
	TDS_2	$TDS_1 + [Cl^-]$
	TDS_3	$[Ca^{2+}] + [K^+] + [Mg^{2+}] + [Si]$
	TDS_4	$[Ca^{2+}] + [Mg^{2+}] + [Si] + [Na^+]$
Salinity	Salt	$[Na^+] + [Mg^{2+}] + [Ca^{2+}]$
Nutrients	Nutri	$[TN] + [NH_4–N] + [TP]$
Metals	Metals	$\Sigma[Sb + As + Ba + Cu + Fe + Li + Mn + Mo + Zn]$

2.5.4. Exploratory Correlation and Visual Assessment

A comprehensive correlation analysis was performed across three datasets: rainy season, dry season, and the full monitoring period. Pearson correlation coefficients were computed between all spectral predictors and water quality parameters. Variables with $|r| > 0.5$ and $p \leq 0.05$ were considered significant and retained for subsequent modeling.

To visually explore these relationships, scatter plots with fitted regression lines and associated R^2 values were generated. These visualizations included the following:

1. Individual spectral bands vs. water quality parameters;
2. Band ratios and transformations;
3. Seasonal comparisons to detect optical response shifts.

This exploratory phase facilitated the interpretation of the physical relationships between the spectral bands and the water quality parameters and the preselection of band combinations for predictive modeling.

2.5.5. Season-Specific Model Training and Validation

Regression modeling was carried out separately for the rainy season and dry season to account for temporal variability in reflectance dynamics.

1. Dry season: All available data points consisting of matched in situ water quality measurements and Sentinel-2 imagery collected between June and September 2018–

2022 were used for model training. An independent dataset from October 2024, provided by the Autoridad Nacional del Agua (ANA) and temporally aligned with a Sentinel-2 acquisition, was reserved exclusively for model validation.

2. Rainy season: The full dataset of paired field and satellite observations from the rainy season was randomly divided into 80% for training and 20% for validation, ensuring separation between calibration and evaluation stages.

2.5.6. Model Construction and Selection

All possible one-to-four band combinations were evaluated using the regression models described in Section 2.5.1. Model performance was assessed based on goodness of fit (R^2), predictive accuracy (RMSE, MAPE), and statistical significance ($p < 0.05$) [51]. The resulting models were categorized as follows: (i) single-band models (e.g., Band 11 predicting TDS), (ii) simple band combinations (e.g., Band 3/Band 11, Band 8 × Band 4), and (iii) composite or index-based models (e.g., MNDWI, WRI1).

2.5.7. Statistical Analysis and Model Performance Assessment

Model performance was quantified using three standard statistical metrics [70,71]:

1. Coefficient of Determination (R^2)—Proportion of variance explained.
2. Mean Absolute Percentage Error (MAPE, %)—Measures prediction accuracy as a percentage:

$$MAPE\% = \sum_{i=1}^{n} \left(\frac{\left| Y_i^{estimated} - Y_i^{measured} \right|}{Y_i^{measured}} \right) * 100\% \quad (8)$$

3. Root Mean Square Error (RMSE)—to measure the average magnitude of the prediction error, expressed in the same units as the parameter evaluated:

$$RMSE = \frac{\sqrt{\sum_{i=1}^{n} \left(Y_i^{estimated} - Y_i^{measured} \right)^2}}{n} \quad (9)$$

3. Results

3.1. Validation of Empirical Water Quality Models with in Situ Observations

Comparison Between Remote Sensing-Derived and in Situ Measurements

Figure 2 compares the temporal dynamics of selected water quality parameters derived from empirical remote sensing models against in situ field measurements. The comparison spans both hydrological seasons (rainy and dry), capturing seasonal variability characteristic of Lake Chinchaycocha's hydro-optical behavior.

Figure 3 summarizes the seasonal model performance for key parameters, reporting the coefficient of determination (R^2) and root mean square error expressed as a percentage (RMSE %).

Complementary validation metrics, including mean absolute error (MAE), bias, *p*-values, sample size, and observed concentration ranges, are detailed in Appendix A, Table A1.

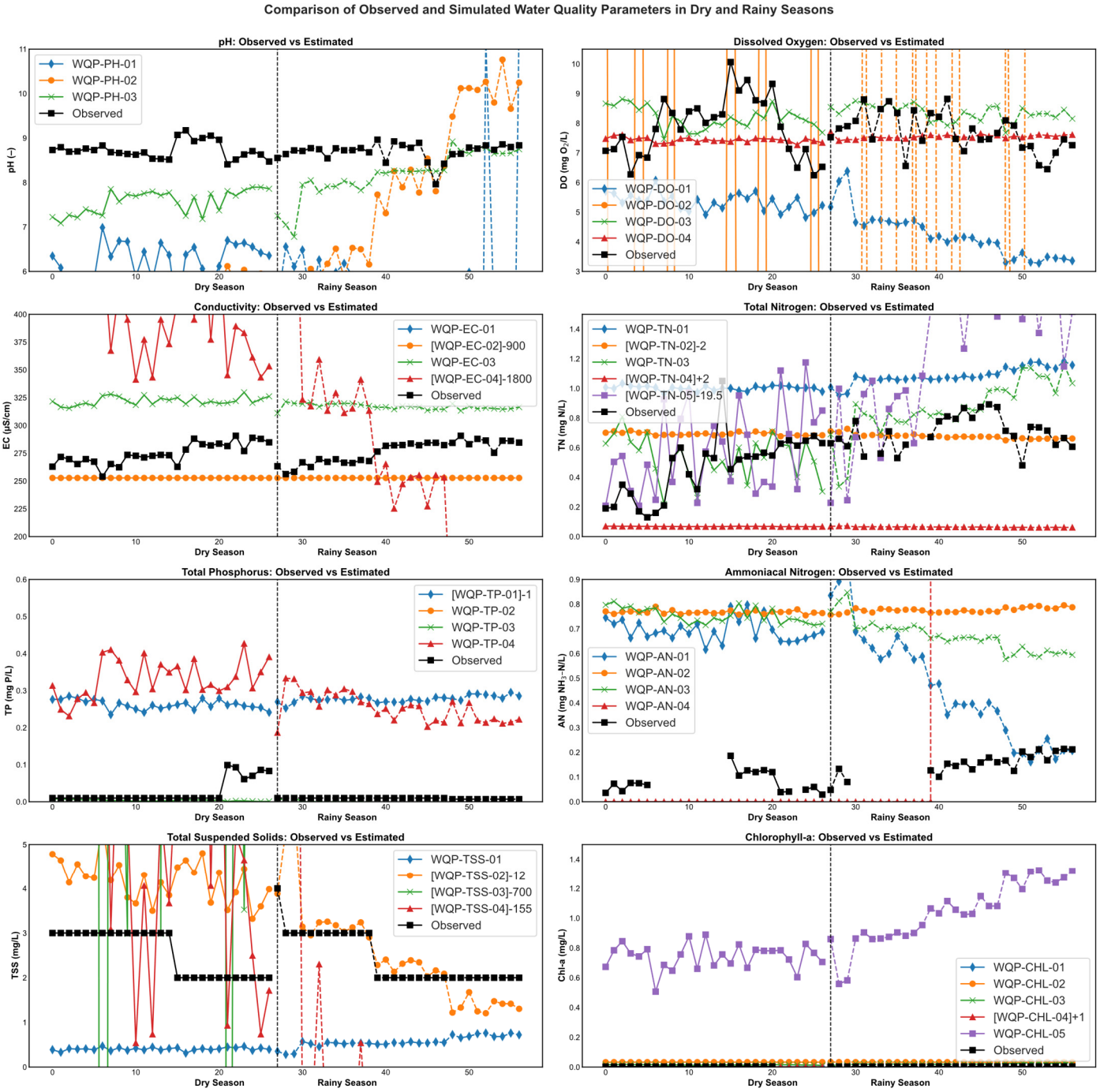

Figure 2. Temporal comparison of water quality estimates derived from remote sensing models versus in situ measurements during the rainy and dry seasons.

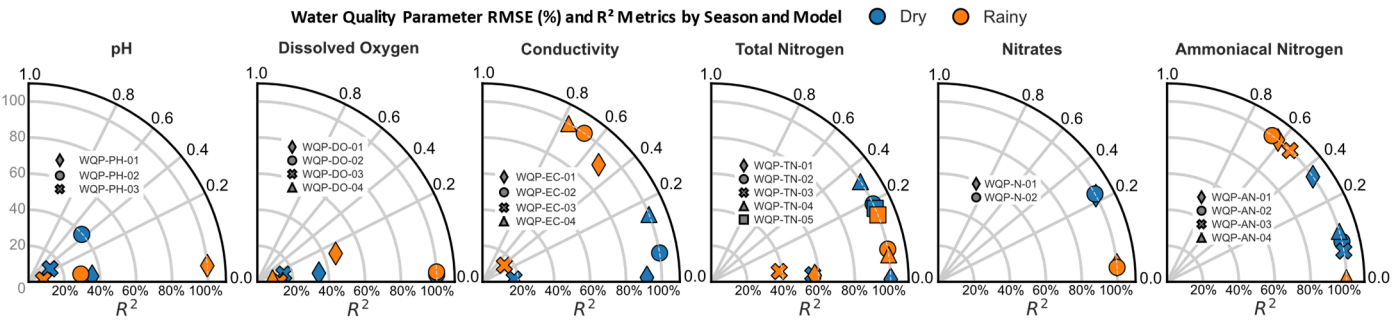

Figure 3. Seasonal model performance for selected parameters, expressed as RMSE (%) and R^2.

3.2. Development of Local Predictive Models for Lake Chinchaycocha

3.2.1. Exploratory Correlation Analysis

(a) Seasonal Reflectance Distribution by Spectral Band

Figure 4 illustrates the seasonal distribution of Sentinel-2 surface reflectance values across spectral bands. These patterns highlight the optical variability associated with seasonal shifts in water quality, suspended material, and surface conditions.

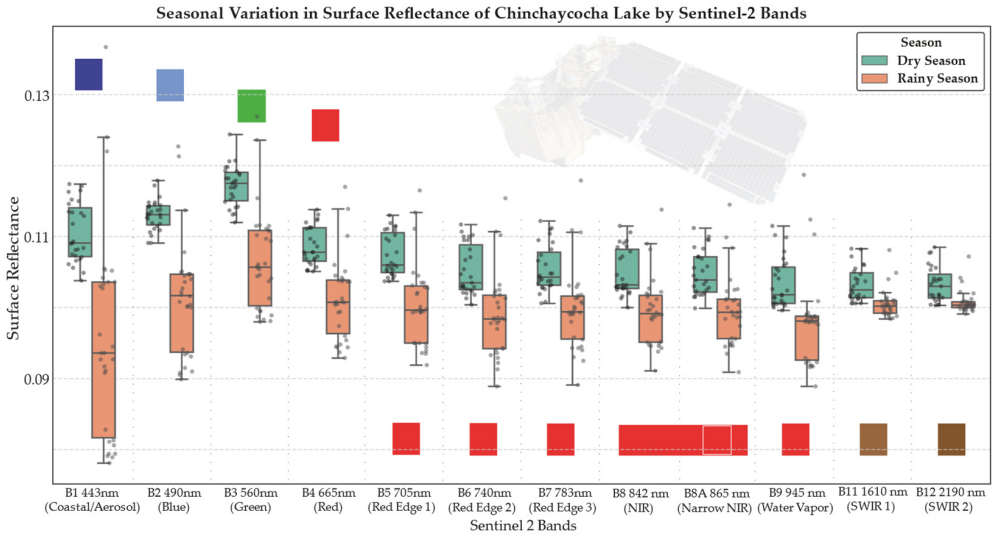

Figure 4. Seasonal distribution of Sentinel-2 surface reflectance values by spectral band in Lake Chinchaycocha.

(b) Pearson Correlation Network among Water Quality Parameters

Figure 5 presents a correlation network for key WQP during both the dry and rainy seasons. Statistically significant Pearson correlations ($|r| \geq 0.5$) are represented by edges, where color indicates direction (positive or negative), and edge width reflects correlation strength. Solid lines denote rainy season correlations, while dashed lines indicate dry season relationships. This network visualization highlights seasonal co-variation, variable clustering, and potential redundancies among all WQP.

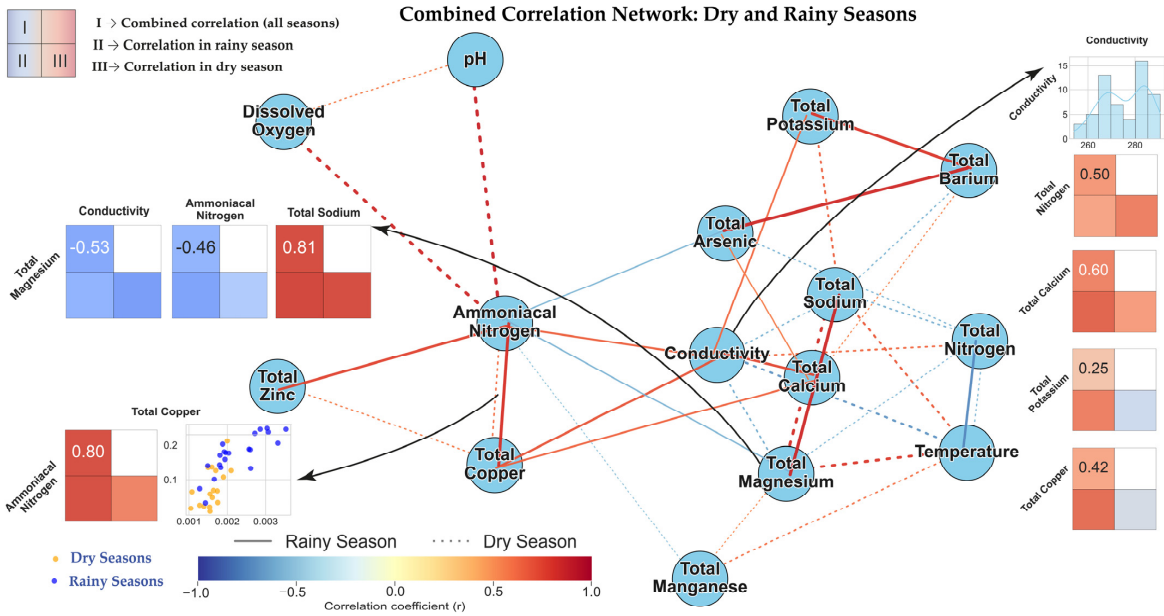

Figure 5. Correlation network of water quality parameters in dry and rainy seasons.

(c) Heatmap of Correlations Between Spectral Bands and Water Quality Parameters

Figure 6 displays heatmaps for the rainy, dry, and full monitoring periods, showing the most relevant spectral bands per season based on Pearson's r and statistical significance ($p < 0.05$) [51]. These visual patterns help identify spectral regions with strong potential for remote sensing–based prediction of specific water quality parameters.

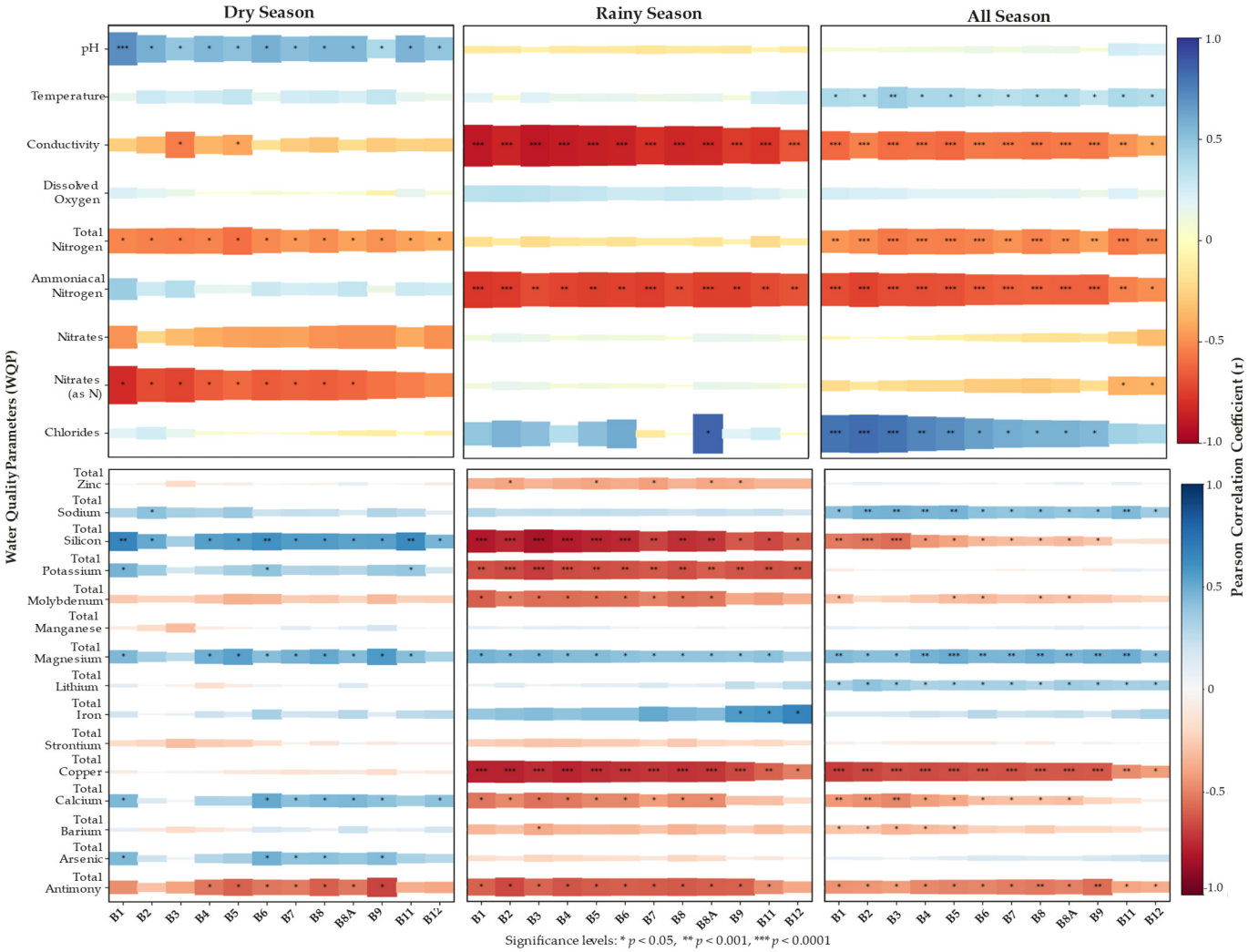

Figure 6. Correlation matrix between Sentinel-2 spectral bands and water quality parameters.

(d) Spider Diagram of Indices

Figure 7 presents spider diagrams comparing R^2 values between spectral indices and water quality parameters, emphasizing seasonal patterns and distinctions across parameter groups (e.g., nutrients, physicochemical attributes, and metals). This visualization enables a comparative assessment of index performance under varying seasonal conditions.

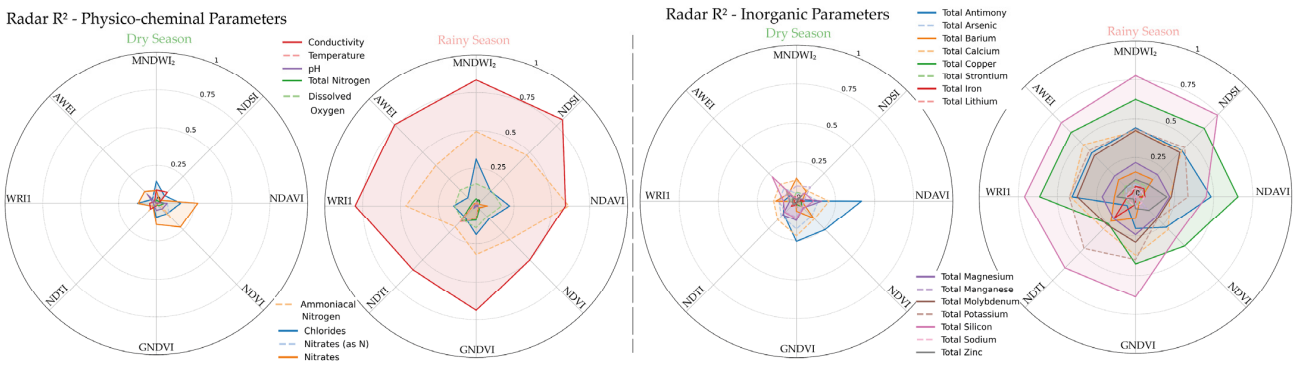

Figure 7. Spider diagram of indices.

3.2.2. Visual Analysis Using Scatter and Bar Charts

Scatter plots with regression lines and R^2 were used to analyze relationships between spectral bands and water quality parameters. Figures 8–10 show individual and combined band scatter plots and seasonal R^2 bar charts.

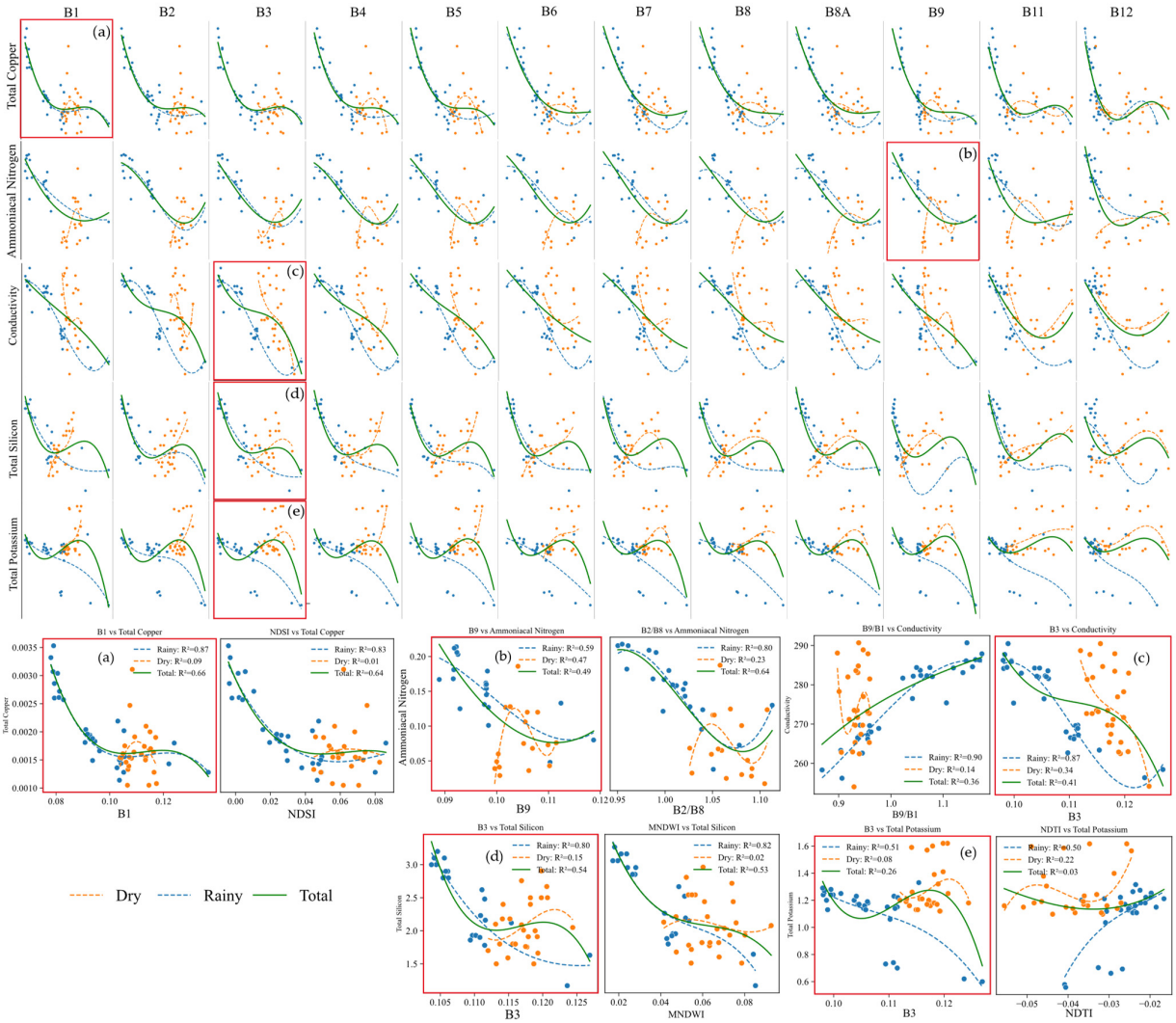

Figure 8. Scatter plots showing the relationship between individual spectral bands and water quality parameters across seasons (dry, rainy, and total). Subfigures (**a**–**e**) show detailed views of selected relationships: (**a**) B1 vs. Total Copper; (**b**) B9 vs. Ammoniacal Nitrogen; (**c**) B3 vs. Conductivity; (**d**) B3 vs. Total Silicon; (**e**) B3 vs. Total Potassium.

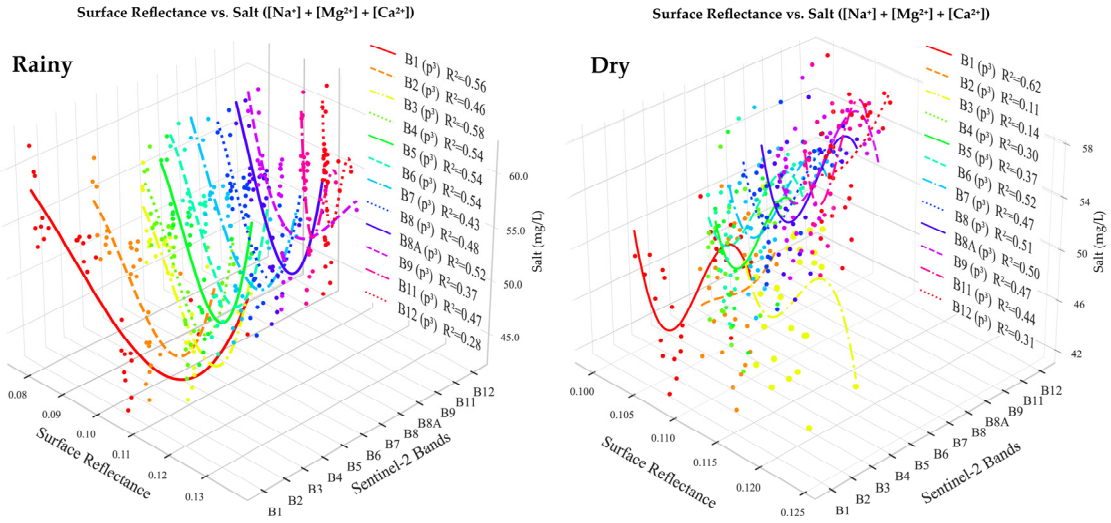

Figure 9. Scatter plots of the best-performing band combination.

(a) Band ratios, products, and other transformations

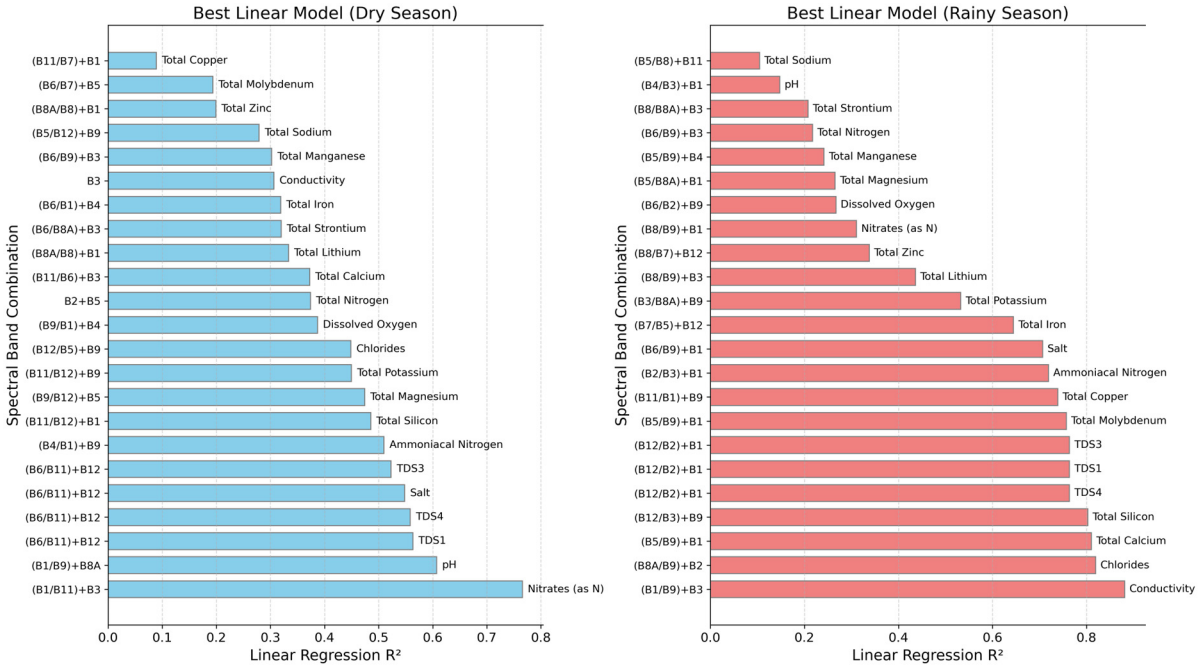

Figure 10. Bar charts of R^2 for top regression band combinations in the dry and rainy seasons.

3.2.3. Derivation of Predictive Equations and Model Validation

To account for seasonal variability in optical responses and water quality dynamics, predictive models were developed separately for the dry and rainy seasons. The best-performing models, selected based on a combination of high R^2 and low RMSE during both training and validation, are presented in Tables 7 and 8. Complete model outputs, including all tested band combinations and functional forms, are provided in Appendix B (Tables A2 and A3).

Table 7. Representative regression models for key water quality parameters during the dry season.

WQP	Band Combination	Model Equation	Train	Test	
			R^2	R^2	RMSE
NH_3–N	(B4/B1) + B9	Polynomial (2°)	0.57	0.03	0.115
Total Calcium	(B11/B6) + B3	Linear	0.37	0.50	2.695
Total Potassium	B1, B7	Linear	0.31	0.63	0.063
Total Silicon	(B11/B12) + B9	Polynomial (3°)	0.51	0.81	0.252
TDS_1	(B6/B11) + B12	Linear	0.56	0.71	4.896
Salt	(B6/B11) + B12	Linear	0.55	0.68	4.798

Table 8. Performance evaluation of regression equations based on selected spectral band combinations for estimating water quality parameters during the rainy season.

WQP	Band Combination	Model Equation	Train	Testing	
			R^2	R^2	RMSE
EC	(B1/B9) + B3	Linear	0.8774	0.91	4.039
NH_3–N	(B2/B3) + B1	Linear	0.84	0.35	0.036
Total Calcium	(B5/B9) + B1	Polynomial (3°)	0.84	0.92	2.350
Total Copper	(B11/B1) + B9	Polynomial (3°)	0.87	0.95	0.0002
Total Lithium	(B8/B9) + B3	Linear	0.45	0.71	0.001
Total Potassium	B3, B5	Linear	0.47	0.82	0.100
Total Silicon	(B12/B3) + B9	Linear	0.76	0.91	0.274
Salt	(B6/B9) + B1	Linear	0.69	0.92	1.101
TDS1	B1, B9	Linear	0.75	0.80	2.012

Figures 11 and 12 illustrate the comparison between observed and predicted concentrations, highlighting the fit and accuracy of the selected models. Shaded areas represent acceptable deviation thresholds.

3.2.4. Long-Term Spatial and Monthly Patterns of Salinity (Salt) in Lake Chinchaycocha

The combined concentration of sodium (Na^+), magnesium (Mg^{2+}), and calcium (Ca^{2+}), hereafter referred to as "Salt", was selected for spatiotemporal analysis due to its ecological, agricultural, and operational significance in Lake Chinchaycocha.

Almost all salts, even at low concentrations, are toxic to certain forms of aquatic life [17]. Salinity is one of the most brutal environmental factors limiting the productivity of crop plants, because most crop species are sensitive to salinity caused by high concentrations of salts in the soil, and the area of land affected by it is increasing day by day [72]. Water corrosivity has caused damage to hydro-mechanical equipment and has reduced production capacity. As water corrosivity has increased, maintenance requirements in hydroelectric facilities have also intensified [73].

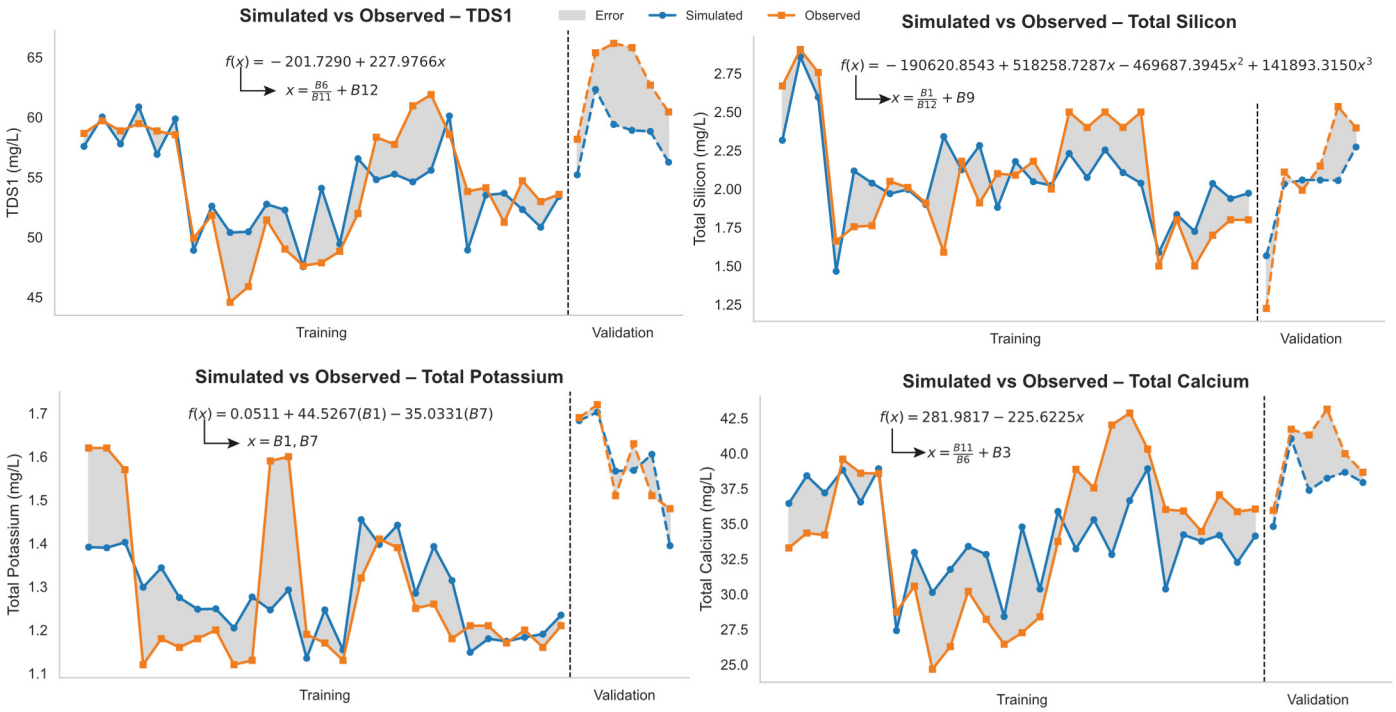

Figure 11. Comparison between observed and predicted values of WQP during the dry season for both training and testing datasets.

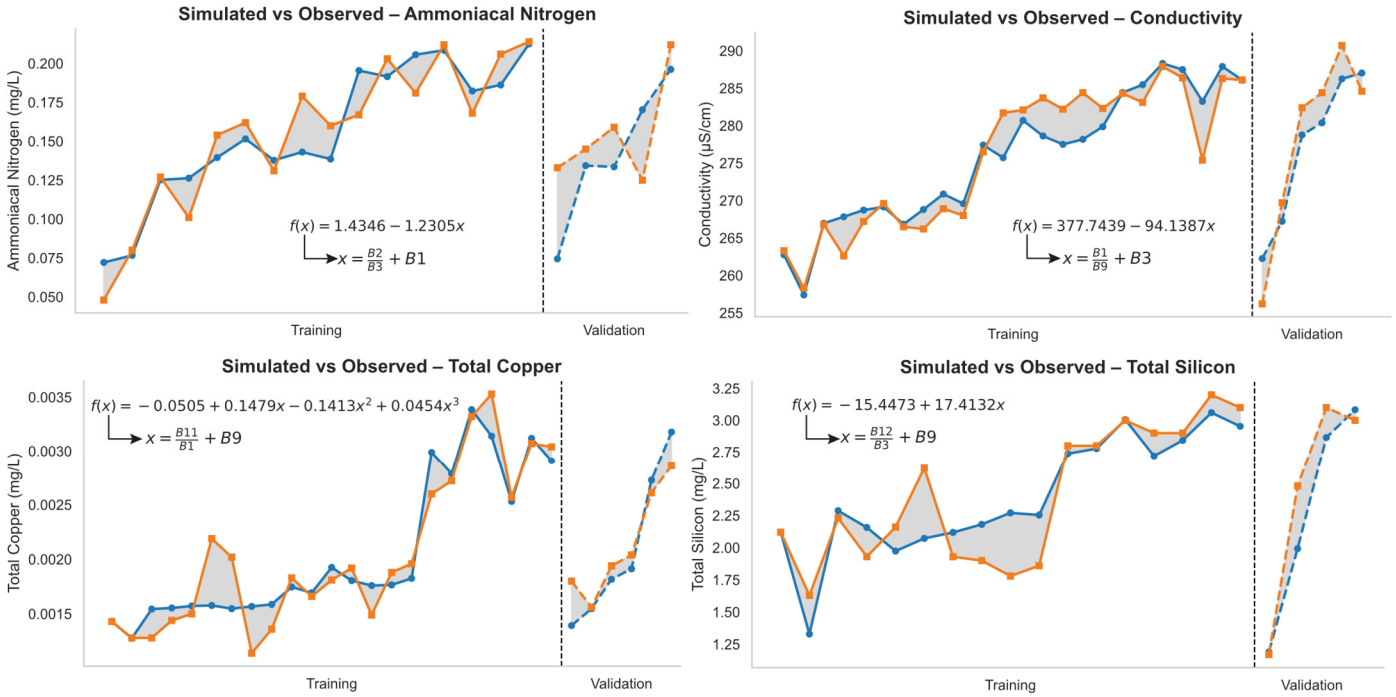

Figure 12. Comparison between observed (orange lines) and predicted (light blue lines) values of water quality parameters during the rainy season for both training and testing datasets.

4. Discussion

4.1. Review of Empirical Algorithm Performance

The use of empirical algorithms developed in ecologically and hydrologically distinct environments remains one of the most persistent limitations in satellite-based water quality modeling [74]. Nonetheless, several studies conducted in tropical and subtropical regions have reported promising outcomes when applying externally developed models. For

instance, Muhoyi et al. [46] successfully implemented TSS, COD, TN, and TP algorithms originally proposed by Song et al. [53], Wang et al. [45], and Torbick et al. [47] in riverine systems of Zimbabwe. Similarly, Kowe et al. [43] reported satisfactory performance when applying chlorophyll-a, turbidity, TSS, and TN models in African reservoirs, suggesting that under certain hydro-optical conditions, empirical model transferability is viable.

By contrast, the present study found that none of the widely cited empirical algorithms tested in Lake Chinchaycocha yielded acceptable predictive performance. Despite being originally calibrated with Sentinel-2 data and exhibiting strong R^2 values in their source ecosystems, all transferred models showed substantial reductions in accuracy, with most presenting near-zero R^2 values and large errors across both dry and rainy seasons. These results emphasize the challenges of applying generalized models to high-altitude, ultraoligotrophic lakes with complex optical and ecological dynamics.

For example, the pH models WQP-PH-01 and WQP-PH-02, developed for the Bajo Sinú wetlands (Colombia) and the Tres Marías Reservoir (Brazil), reported R^2 values between 0.84 and 0.89 in their original studies [37,38]. However, when applied to Chinchaycocha, both models performed poorly, indicating a complete breakdown in predictive utility under local conditions.

Electrical conductivity (EC) models, including WQP-EC-01 (NDSI-based) [40], WQP-EC-02 (B2, B5, B6) [7], WQP-EC-03 (band ratios B5/B3 and B7/B8) [37], and WQP-EC-04 (B4-based) [39], exhibited high seasonal sensitivity. Moderate-to-strong correlations were observed during the rainy season (R^2 = 0.36–0.77), but model performance declined sharply in the dry season (R^2 < 0.15), with RMSE values ranging from 253 to over 1900 µS/cm. These variations likely reflect seasonally driven changes in ionic concentrations, evaporation, and hydrological dilution, factors that influence the spectral behavior of salinity. Given differences in EC ranges among sites, caution is advised when comparing RMSE values with those reported in the original model contexts.

Models for dissolved oxygen (DO), including WQP-DO-01 to WQP-DO-04, which previously demonstrated R^2 values between 0.56 and 0.85 [3,37,38,41], showed poor performance in Chinchaycocha, with negligible R^2 values and markedly inflated RMSE. This result is consistent with the well-known limitation of DO as a remote sensing target due to its lack of direct optical absorption features. Additionally, consistently low chlorophyll-a concentrations (<0.0041 mg/L), as reported by the Peruvian Autoridad Nacional del Agua (ANA) between 2016 and 2024, indicate ultraoligotrophic conditions with limited primary productivity and, consequently, low photosynthetic oxygen generation—further reducing the feasibility of remote DO estimation.

Chlorophyll-a models proved equally unviable. All laboratory measurements across field campaigns were below detection thresholds, indicating negligible phytoplankton biomass. Unsurprisingly, models developed for eutrophic and hypereutrophic systems, such as those for Lake Burullus and the Tres Marías Reservoir [33,71,75–77], produced nonphysical outputs (e.g., negative or zero concentrations). In ultraoligotrophic systems like Chinchaycocha, the remote estimation of chlorophyll-a is virtually unattainable outside of anomalous bloom events.

Similarly, total suspended solids (TSS) presented severe limitations. With only one field measurement exceeding the detection limit (<2 mg/L), reliable validation of empirical models was not possible. However, model WQP-TSS-01 provided spatially coherent estimates, potentially reflecting episodic particulate matter associated with localized hydrometeorological events.

In terms of nutrients, total nitrogen (TN) models, originally showing R^2 values up to 0.6 in nutrient-rich systems [3,42,43,46,47,49], yielded low accuracy and high prediction errors in Chinchaycocha. Nitrogenous compounds, specifically nitrates and ammoniacal

nitrogen (NH_3–N), also exhibited poor transferability. Nitrate models returned R^2 values below 0.3 [41,52], and although some NH_3–N models achieved R^2 values between 0.5 and 0.8 during the rainy season, performance dropped substantially in the dry season, with RMSE% exceeding 100% [3,49–51].

Finally, even spectrally conservative ions, such as sodium (Na^+), chloride (Cl^-), and magnesium (Mg^{2+}), which are generally less influenced by biological variability and are considered more stable across sites [7,40], failed to perform adequately in Chinchaycocha. R^2 values remained below 0.25 and RMSE values were persistently high (Appendix A Table A1). These results suggest that local mineralogy, co-occurring optical constituents, and watershed-specific hydrodynamics introduce sufficient variability to impair even the most robust empirical models, reinforcing the necessity of local recalibration for operational use.

4.2. Physical and Spectral Relationships Between Sentinel-2 Bands and Water Quality Parameters

4.2.1. Seasonal Variability in Sentinel-2 Reflectance

Figure 4 shows a clear seasonal contrast in surface reflectance in Lake Chinchaycocha, with consistently higher values across all Sentinel-2 bands during the dry season (May–September). This period is characterized by reduced rainfall, limited fluvial inflows, and lower water levels [78], leading to greater optical clarity and increased reflectance, particularly in B2 (blue) and B3 (green), which are sensitive to light scattering by mineral particles in clear waters [71,79].

During the dry season, reduced inputs of suspended sediments and organic matter decrease absorption by chlorophyll-a and CDOM, enhancing reflectance in the visible range [71,80]. These patterns are consistent with observations in other high-altitude lakes, where maximum transparency typically occurs in the dry season [71].

In contrast, the rainy season (November–March) exhibits a sharp drop in reflectance across all bands due to increased runoff and the influx of dissolved organic matter (DOM), especially humic and fulvic acids, which absorb strongly at short wavelengths [79]. This effect is most notable in B2 and B3, which showed significantly lower reflectance during this period.

Similar seasonal optical transitions have been documented in other Andean lakes. For example, in Lake Pacucha (Peru), the apparent color of surface waters shifts from green-blue in the dry season to reddish-brown in the wet season, driven by increased CDOM and suspended solids. These changes have been quantitatively linked to precipitation levels [81].

These seasonal trends in optical response are further supported by studies on CDOM dynamics. Alcântara et al. [82] observed elevated aCDOM(440) during the dry season in a eutrophic tropical lake, while Coelho et al. [79] emphasized the role of thermal stratification and water residence time as modulators of CDOM accumulation. In large lakes like Chinchaycocha, such mechanisms may be enhanced by increased column stability during the dry season.

Band 1 (ultra-coastal, 443 nm) exhibited the highest seasonal variability, responding primarily to atmospheric conditions such as aerosols, mist, and hygroscopic salts, particularly during the rainy season. Its more stable signal during the dry period indicates lower atmospheric interference and reduced surface deposition of chlorides and sulfates.

4.2.2. Relationships Among in Situ Water Quality Parameters

Figure 5 reveals consistent groupings among physicochemical parameters. Electrical conductivity (EC) was strongly associated with major dissolved ions, sodium (Na^+), magnesium (Mg^{2+}), and chloride (Cl^-), reflecting its role as an indicator of total ionic

load [83]. This relationship was particularly strong during the dry season, when increased evaporation elevates solute concentrations. These trends also align with Table 1, which details seasonal variability in water chemistry.

Such associations mirror findings from other Andean lakes such as Pacucha, where near-linear correlations between EC and total dissolved salts have been attributed to concentration during low-flow conditions [81]. In limnology, these are well-established consequences of low hydrological turnover and increased ionic accumulation during the dry season.

A key finding was the strong positive correlation between ammoniacal nitrogen (NH_3–N) and total copper (Cu), with r = 0.80 during the rainy season, r = 0.59 in the dry season, and r = 0.80 overall. This suggests a shared origin, likely associated with agricultural, mining, or urban sources [84], and indicates active biogeochemical interactions within the water column, particularly under high organic loads or sediment disturbance.

Ecologically, copper can disrupt the nitrogen cycle by inhibiting nitrification and ammonification at the sediment–water interface [85]. During the rainy season, sediment resuspension may release bound copper, increasing its bioavailability and its interaction with reduced nitrogen. Both Cu and NH_3–N can form complexes with dissolved organic matter (DOM), affecting their mobility and toxicity. While Cu tends to bind with humic and fulvic fractions, NH_3–N is influenced by pH, temperature, and colloidal conditions, resulting in a seasonally dynamic speciation equilibrium.

The persistent correlation between Mg^{2+}, Na^{+}, and Cl^{-} further supports a dominant geogenic origin, likely from the dissolution of igneous material, evaporites, or saline soils in the basin [81]. The stability of these relationships underscores their potential as baseline hydrochemical indicators.

In summary, the correlation network indicates two dominant processes: (i) concentration of salts during the dry season due to hydroclimatic drivers, and (ii) co-input of nutrients and trace metals from anthropogenic sources. Interpreting water quality in such systems requires both robust in situ datasets and an understanding of the limnological and geochemical processes at play. Although in situ monitoring is often costly, time-consuming, or logistically limited [71], historical databases can provide a valuable foundation for remote sensing-based assessments.

4.2.3. Spectral Relationships Between Sentinel-2 Bands and Water Quality Parameters

This section integrates statistical correlations between Sentinel-2 reflectance bands and water quality parameters, categorized as dissolved salts and TDS, nutrients, and metals. Analyses emphasize seasonal contrasts and indirect optical mechanisms, as shown in Figures 6–10.

1. Electrical Conductivity and Major Ions

During the rainy season, EC exhibited significant negative correlations ($r < -0.5$, $p < 0.05$) across nearly all visible and NIR bands (B1–B8A), particularly B3 (560 nm), B4 (665 nm), and B8A (865 nm). This response was less pronounced in the dry season, where only B3 and B5 remained significant.

This trend is consistent with oligotrophic high-altitude systems where low algal biomass and negligible CDOM allow clearer detection of ionic absorption effects. In Chinchaycocha, chlorophyll-a and SST were below the detection limits of laboratory instrumentation, reinforcing the predominance of indirect reflectance drivers. Similar dynamics were observed in Lake Atillo, Ecuador (CHL = 0.16 ± 0.1 mg/m^3) [71].

The inverse reflectance–EC relationship is physically explained by increased refractive index and radiation absorption due to ions like Ca^{2+}, Mg^{2+}, and Cl^{-}, especially in red and NIR wavelengths [1]. This dielectric attenuation has been well documented in mineralized

freshwater systems [83]. Similar negative correlations were observed for ammoniacal nitrogen, silicon, potassium, molybdenum, copper, calcium, and antimony during the rainy season, likely driven by runoff-enhanced ion input and optical path alteration [1].

Interestingly, magnesium displayed a positive correlation, possibly due to differences in its scattering behavior or complexation effects under local conditions.

2. Nutrients and trace metals (copper and ammonia nitrogen)

NH_3–N and Cu presented notable spectral behavior during the rainy season, showing significant correlations with B2–B4 and B8. While NH_3–N has previously shown indirect associations with phytoplankton-driven reflectance in eutrophic systems [3,49–51], this mechanism is not applicable in Chinchaycocha due to negligible Chl-a and TSS levels.

In this ultraoligotrophic context, both parameters likely exhibit optical detectability via co-mobilization with optically active fractions (TDS, organic colloids, suspended sediments) [86,87]. Their high mutual correlation across seasons ($r \approx 0.8$ wet, $r \approx 0.5$ dry) further supports a shared source, potentially agricultural or mining runoff [84].

These results highlight the indirect spectral expression of NH_3–N and Cu, governed by hydrodynamics and co-occurrence with active constituents. This is consistent with recent remote sensing studies of trace metal and nutrient detection in optically complex waters [88].

3. Spectral Behavior of Additional Metals and Ions

Among trace elements, calcium, potassium, and silicon exhibited the strongest correlations, particularly in the B5–B12 region and in band ratios such as B6/B11 and B11/B12. These ions are major TDS contributors and displayed spectral responses similar to EC. Models using these ratios performed well ($R^2 > 0.6$), especially during the dry season (Tables 7 and 8).

Heavier metals (e.g., Cu, Zn, Mo, Sb) yielded statistically significant but weak correlations ($r < 0.4$), suggesting either indirect associations or detection limitations at the observed concentrations. Copper's detectability also varied seasonally. In dry months, Cu likely precipitates and accumulates in sediments, limiting its spectral signature. During the rainy season, turbulence and sediment resuspension redistribute Cu to surface layers, enhancing its interaction with visible and NIR wavelengths. Its tendency to complex with DOM alters both mobility and spectral response, potentially leading to synergistic or masking effects.

4. Atmospheric Effects on Band 1 (443 nm)

Band 1 (443 nm) showed positive correlations with several parameters, including EC, Cu, and potassium. However, this band is known for its high sensitivity to atmospheric interference, particularly aerosols, water vapor, and submicron suspended particles, which is especially relevant during the rainy season [81]. This optical instability complicates the interpretation of B1 reflectance, as spectral signals may conflate aquatic chemistry with atmospheric variability.

While Band 1 has demonstrated utility in modeling certain water quality parameters, its use as a predictor must be approached with caution. In the literature, B1 is often employed for atmospheric correction purposes due to its strong interaction with Rayleigh scattering, and it is explicitly corrected in preprocessing algorithms such as Sen2Cor (for surface reflectance Level-2A products) and ACOLITE (targeting coastal and inland waters). These tools account for atmospheric distortions by modeling aerosol properties and path radiance.

In the present study, we used Sentinel-2 imagery at Level-2A, already atmospherically corrected using the Sen2Cor algorithm. However, no additional validation or adjustment of B1 reflectance was conducted beyond the default preprocessing. This represents a

methodological limitation, particularly when using B1 as an explanatory variable. Future work should incorporate aerosol optical thickness data and cross-reference with ACOLITE-derived water-leaving reflectance to validate B1 performance in optically complex, high-altitude environments. Integrating humidity indices or correction layers is strongly recommended to minimize confounding effects and avoid misleading empirical inferences.

4.3. Evaluation and Calibration of Models with in Situ Data

In Chinchaycocha, salts (composite indices of Na^+, Mg^{2+}, and Ca^{2+}) were the most robust parameters in both the dry and wet seasons. During the dry season, models yielded moderate R^2 values for NH_3–N (~0.57), total calcium (~0.35–0.37), total potassium (~0.31–0.45), total silica, TDS_1, and salinity, with RMSE and MAE consistent with field-measured ranges. In the wet season, models for EC, NH_3–N, total calcium, total copper, total lithium, total potassium, total silica, salinity, and TDS_1 performed even better ($R^2 > 0.6$ in most cases), both in training and validation (see Annexes B1 and B2).

Parameters such as DO and pH, although showing significant correlations in training (R^2 between 0.3 and 0.5), failed during testing, with R^2 values close to zero and high absolute errors. This is likely due to their low optical activity, which limits satellite-based detection under ultraoligotrophic conditions.

The best-performing equations employed multiband combinations involving visible (B1–B4), red-edge, and SWIR bands (B11–B12). For example, NH_3–N was modeled using (B4/B1 + B9), leveraging red–infrared contrast; total calcium with (B11/B6 + B3); potassium with (B11/B12 + B9); and salinity with (B6/B11 + B12). These spectral indices follow common empirical modeling strategies. The inclusion of B1 may indirectly reflect atmospheric moisture and high-Andean aerosols associated with mineral mobilization during rainfall. This is consistent with findings linking visible bands to surface composition and CDOM [89]. Separately, SWIR bands (especially B11 and B12) are often associated with turbidity, dissolved matter, and metal absorption features. For instance, the B11/B6 ratio—also used here for calcium—has been identified as effective for detecting copper in pluvial environments due to SWIR–red contrast [90]. Although models were attempted for trace metals such as Al, As, and Sb, no reliable equations were achieved. This is likely due to their extremely low concentrations in Chinchaycocha (in the μg/L range), which generate minimal optical contrast. These results support the broader conclusion that optically active parameters, such as turbidity, CDOM, and chlorophyll-a, are more reliably estimated using satellite imagery than inorganic nutrients or trace metals at low concentrations.

Additionally, Figure 13 presents the simulated vs. observed comparison of salinity in training and validation for both seasons, along with monthly spatial distribution maps. The model accurately reproduces seasonal trends, capturing salinity increases during rainy peaks and decreases in the dry season. In September 2024, the highest salinity peak in the lake was recorded, which has ecological, agricultural, and hydraulic implications [17,72,73]. This event coincides with the end of the dry season, when accumulated evaporation and reduced inflow can concentrate dissolved salts. The satellite maps show strong spatial consistency in predictions: the highest concentrations were located in the northeastern margin during May 2024, reflecting fluvial inflows.

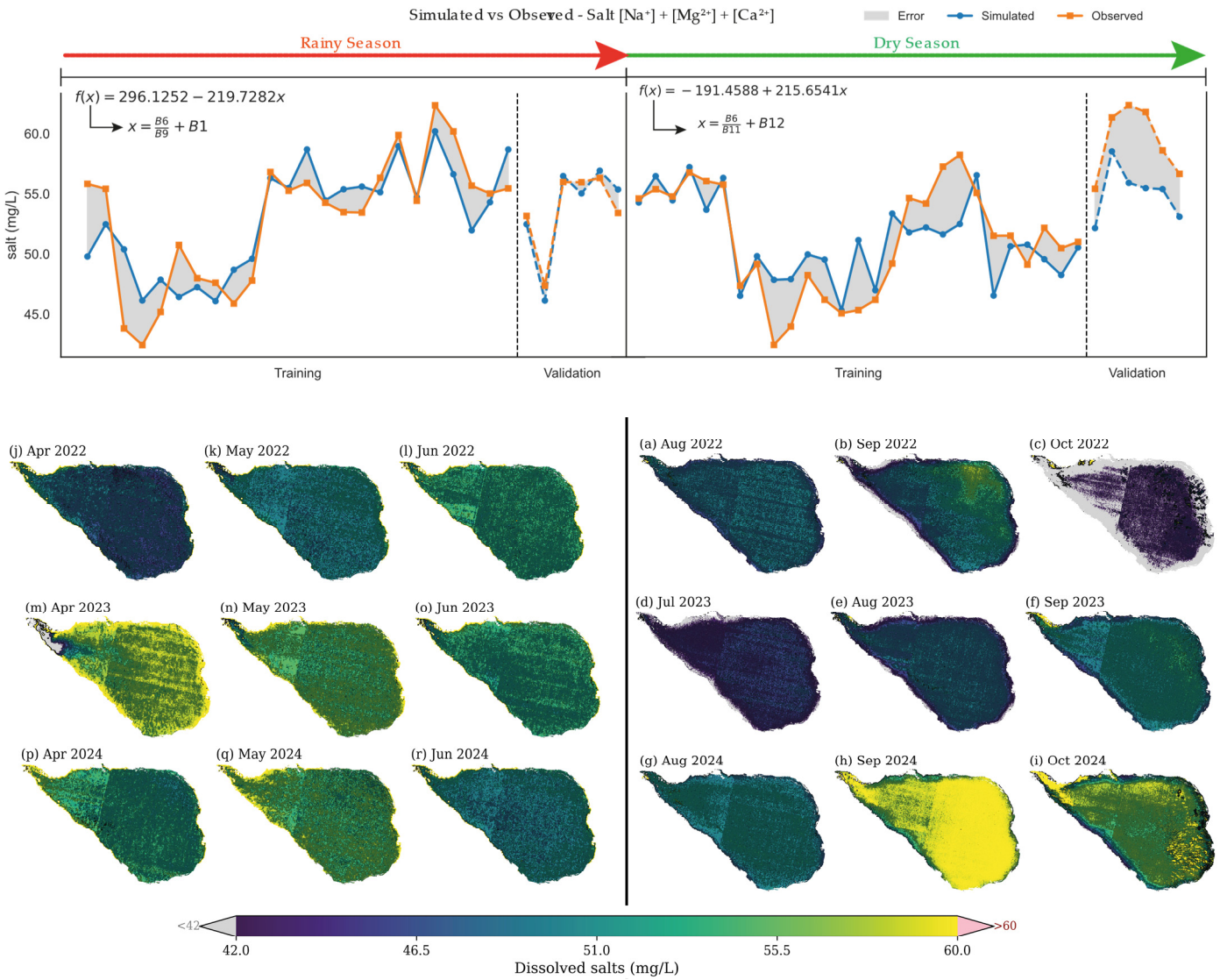

Figure 13. Long-Term Spatial and Monthly Patterns of Salinity (Salt) in Lake Chinchaycocha.

4.4. Ecological and Management Implications of Remote Sensing-Based Water Quality Monitoring Using Governmental Data

Lake Chinchaycocha, a Ramsar-designated site in the high Andes, is affected by three major anthropogenic stressors that compromise its ecological integrity. First, decades of mining activity via the San Juan River have introduced substantial loads of heavy metals (As, Cu, Zn, Pb, Hg) into littoral sediments, leading to bioaccumulation in benthic prey and threatening endemic fauna such as the Junín grebe (*Podiceps taczanowskii*) and the Junín frog (*Batrachophrynus macrostomus*). Other sensitive species, including the Andean condor (*Vultur gryphus*) and the black rail (*Laterallus tuerosii*), are also impacted by metal toxicity and habitat degradation [16,17].

Second, runoff from agricultural areas, rich in nutrients and pesticides, drives eutrophication, while untreated urban effluents (phosphates, detergents, chlorinated by-products) further reduce dissolved oxygen, alter pH and conductivity, and disrupt planktonic communities that underpin the aquatic food web [25]. Third, the convergence of mining legacies, highland agriculture, and expanding urban settlements creates spatially heterogeneous contamination patterns that require high-resolution, continuous environmental monitoring.

Extreme pH values are of particular concern, as they are known to impair amphibian development. According to Castillo et al. [18], mining-impacted tributaries exhibited highly

acidic conditions (pH 2.8–6.2), while alkaline peaks of up to 10.02 were recorded in the lake's northern sector, both extremes posing critical risks to *T. macrostomus larvae*.

Our analysis of 31 physicochemical parameters, including EC, TDS, dissolved oxygen, BOD_5, TN, TP, and multiple trace metals, reveals distinct seasonal trends. During the dry season, reduced hydrological dilution leads to higher concentrations of metals and nutrients; conversely, the rainy season brings increased turbidity and CDOM due to intensified runoff and soil erosion. Coordinating Sentinel-2 L2A satellite overpasses with field-based sampling campaigns enhances temporal alignment, improves model calibration, and strengthens the ecological validity of remote sensing outputs, especially in Peru's sharply contrasting hydroclimatic zones [74,89].

Despite their scientific value, high-quality laboratory-accredited datasets generated by the Autoridad Nacional del Agua (ANA) remain underexploited in satellite-based water quality assessments. Coupling these in situ observations with spectral data enables the development of context-specific predictive models and supports the creation of a unified geospatial data platform across key institutions, including ANA, OEFA, SENACE, and SENAMHI. Additionally, it is essential to establish a centralized repository of monitoring data collected by private companies under the commitments outlined in their Environmental Management Instruments. This would help address existing spatial and temporal data gaps while fostering public–private collaboration.

Recent OEFA reports reveal that 100% of sediment samples collected in June exceeded Canadian ISQG (5.9 mg kg^{-1}) and PEL (17 mg kg^{-1}) guidelines for total arsenic. In the same period, 75% of surface water samples surpassed Zn limits and 15% exceeded thresholds for Cu, Pb, and Hg—with similarly elevated levels recorded in September [84]. These findings reinforce the need for continuous, year-round monitoring and the implementation of stricter effluent discharge controls.

To translate these findings into actionable policy, we emphasize the need to (i) create a centralized, georeferenced environmental dataset that synthesizes laboratory test reports and water quality data not only from Peru's National Water Observatory (Autoridad Nacional del Agua, ANA), but also from regulatory supervision and assessment campaigns led by OEFA, and from monitoring reports submitted by private companies as part of their environmental surveillance plans mandated by Environmental Management Instruments and reported to agencies such as the Ministry of Production (Ministerio de la Producción, PRODUCE), the Ministry of Agrarian Development and Irrigation (Ministerio de Desarrollo Agrario y Riego, MIDAGRI), and the Ministry of Transport and Communications (Ministerio de Transportes y Comunicaciones, MTC). This dataset should also incorporate other environmental matrices, such as air quality (including records from the National Meteorology and Hydrology Service of Peru, SENAMHI) and biodiversity monitoring results derived from corporate commitments, to form a comprehensive and interoperable metadata framework. Making these datasets accessible and standardized for upload to global research platforms such as GBIF would enhance transparency and enable comparative ecosystem analysis across sectors and regions. Additionally, we recommend (ii) aligning field sampling with Sentinel-2 overpasses to improve temporal coherence; (iii) enforcing stricter discharge limits for pollutants in tributaries feeding Lake Chinchaycocha; and (iv) developing public dashboards that integrate satellite indices and in situ data to support community-level awareness and evidence-based environmental governance. Taken together, these strategies would establish a robust, multisource information infrastructure to strengthen the protection and sustainable management of Lake Chinchaycocha and other high-Andean ecosystems.

5. Conclusions

In this work, we have demonstrated that the blanket application of widely cited empirical algorithms, calibrated in tropical or eutrophic contexts, to the ultra-oligotrophic, optically clear waters of Lake Chinchaycocha yields consistently poor performance across all measured parameters. Weak optical signatures in clear waters, especially during the dry season when minimal inflows and particle loads prevail, impede the accurate retrieval of variables such as pH, dissolved oxygen, chlorophyll-a, and others. Conversely, the rainy season's enhanced runoff and organic-mineral inputs amplify water-column reflectance and dramatically improve statistical correlations, with R^2 often exceeding 0.9 for nutrients, major ions, and select trace metals. This clear seasonal dichotomy underscores the necessity of embedding remote-sensing models within the bio-optical and hydrological realities of high-altitude ecosystems rather than relying on off-the-shelf algorithms.

By developing locally calibrated, season-stratified regression models based on Sentinel-2 visible, NIR, and SWIR bands, we achieved robust predictions for a comprehensive suite of constituents, ranging from electrical conductivity and total dissolved solids to ammoniacal nitrogen, total nitrogen, calcium, potassium, chloride, and several trace metals. The dry season's superior water clarity elevated reflectance in the blue and green bands, while the wet season's particulate and CDOM loads extended model applicability across additional wavelengths. Nonetheless, our approach revealed that purely empirical band selections, although statistically significant, sometimes lack a firm physical rationale, highlighting the importance of integrating bio-optical theory and aerosol correction data to guard against overfitting and to ensure reproducible results.

Our correlation network further clarified two dominant hydrological and anthropogenic processes: (i) ionic concentration during the dry season, driven by evaporation and low flow—responsible for tight groupings among EC, Mg^{2+}, Na^{+}, and Cl^{-}—and (ii) co-mobilization of nutrients and metals during peak runoff, evidenced by the strong NH_3-N–Cu relationship ($r \approx 0.8$), reflecting shared agricultural and mining sources. These insights attest to the multifactorial nature of water-quality dynamics in Andean lakes and reinforce the imperative of pairing spectral analyses with comprehensive in situ chemical and ecological monitoring.

Operationally, the synergy between Sentinel-2 Level-2A imagery, preprocessed with Sen2Cor, and high-quality governmental datasets (ANA, SENAMHI, OEFA, SENACE) provides a cost-effective, scalable framework for continuous water-quality surveillance across Peru's diverse aquatic systems. Tight temporal alignment (± 3 days) between satellite overpasses and field campaigns enhances model validation and allows near-real-time support for management decisions. However, careful handling of atmospheric-sensitive bands (notably B1 at 443 nm) and potential cross-validation with ACOLITE or aerosol optical thickness data are essential to minimize confounding influences.

Looking ahead, we advocate for the institutionalization of sustained, state-supported monitoring programs that employ seasonally adapted, locally validated remote-sensing algorithms. Future research should extend this framework to other Andean and global high-altitude lakes, explore hyperspectral and machine-learning approaches to capture nonlinear, multisensor relationships, and develop long-term time-series analyses to detect climate-driven and anthropogenic trends. Concurrently, ecological and socio-economic impact assessments, focused on species at risk and community water uses, will be critical to translate spectral insights into actionable thresholds for conservation and resource management.

Ultimately, this study offers both a critical appraisal of algorithm transferability and a practical blueprint for advancing the science and governance of high-altitude freshwater ecosystems. By weaving together season-specific empirical models, rigorous in

situ validation, and interinstitutional data integration, we lay the groundwork for robust, transparent, and adaptive water-quality monitoring strategies that can safeguard the ecological integrity and sustainable development of Lake Chinchaycocha and analogous water bodies worldwide.

Author Contributions: Conceptualization, E.E., A.B. and N.R.; Analysis E.E.; Resources E.E.; writing—original draft preparation, E.E., A.B. and N.R.; writing—review and editing, E.E., A.B. and N.R.; visualization, E.E.; supervision, N.R. All authors have read and agreed to the published version of the manuscript.

Funding: The authors express their sincere thanks to the Vicerrectorado de Investigación of the Universidad Nacional de Ingeniería (UNI), Lima, Peru, for supporting the publication of this research.

Data Availability Statement: Dataset supporting the reported results of the study are available on request from the first author.

Acknowledgments: The author sincerely thanks the Autoridad Nacional del Agua (National Water Authority of Peru, ANA), particularly the Autoridad Administrativa del Agua de la Cuenca del Río Mantaro (Administrative Authority of the Mantaro River Basin), for providing the official water quality data used in this study. These data were obtained through a public information request in accordance with the Peruvian Law on Transparency and Access to Public Information.

Conflicts of Interest: The authors declare no conflicts of interest.

Abbreviations

The following abbreviations are used in this manuscript:

R^2	Coefficient of Determination
RMSE	Root Mean Square Error
MAPE	Mean Absolute Percentage Error
CDOM	Colored Dissolved Organic Matter
SWIR	Short-Wave Infrared
Sen2Cor	Sentinel-2 Atmospheric CORrection processor
ACOLITE	Atmospheric Correction for OLI "lite"
COD-Mn	Chemical Oxygen Demand (permanganate method)
pH	Potential of Hydrogen (dimensionless)
EC	Electrical Conductivity
TDS	Total Dissolved Solids
LOQ	Limit of Quantification
NH_3–N	Ammoniacal Nitrogen
NDVI	Normalized Difference Vegetation Index
NDWI	Normalized Difference Water Index
MNDWI	Modified Normalized Difference Water Index
CONAGUA	National Water Commission (Comisión Nacional del Agua, Mexico)
SENAMHI	National Service of Meteorology and Hydrology of Peru (Servicio Nacional de Meteorología e Hidrología del Perú)
MINAM	Ministry of the Environment (Ministerio del Ambiente, Peru)
MIDAGRI	Ministry of Agrarian Development and Irrigation (Ministerio de Desarrollo Agrario y Riego, Peru)
PRODUCE	Ministry of Production (Ministerio de la Producción, Peru)
MTC	Ministry of Transport and Communications (Ministerio de Transportes y Comunicaciones, Peru)
MINEM	Ministry of Energy and Mines (Ministerio de Energía y Minas, Peru)
SERNANP	National Service of Natural Protected Areas (Servicio Nacional de Áreas Naturales Protegidas por el Estado, Peru)
ANA	National Water Authority (Autoridad Nacional del Agua, Peru)

Appendix A

Table A1. Statistical summary of simulated and in situ water quality parameters.

Variable	Code	Season	R^2	RMSE	MAE	Bias	*p*-Value	n	Observed Range
pH	WQP-PH-01	Rainy	0.01	8.76	5.59	−5.23	0.6387	30	−27.856–11.756
		Dry	0.01	3.11	2.75	−2.75	0.6643	27	−0.842–6.987
	WQP-PH-02	Rainy	0.02	2.56	1.96	−1.18	0.4408	30	0.979–10.765
		Dry	0.44	3.46	3.4	−3.4	0.0002	27	4.449–6.119
	WQP-PH-03	Rainy	0.02	0.73	0.56	−0.52	0.4770	30	6.780–8.923
		Dry	0.27	1.22	1.16	−1.16	0.0060	27	7.085–7.895
Conductivity (EC)	WQP-EC-01	Rainy	0.50	253.25	253.07	−253.07	0.0000	30	22.932–23.432
		Dry	0.00	251.75	251.57	−251.57	0.8951	27	22.618–23.301
	WQP-EC-02	Rainy	0.68	876.56	876.51	876.51	0.0000	30	1152.75–1152.77
		Dry	0.03	878.22	878.17	878.17	0.4242	27	1152.75–1152.76
	WQP-EC-03	Rainy	0.36	42.22	40.66	40.66	0.0004	30	311.06–321.34
		Dry	0.01	48.63	47.52	47.52	0.6608	27	315.56–329.78
	WQP-EC-04	Rainy	0.77	1791.81	1787.64	1787.64	0.0000	30	1897.30–2379.30
		Dry	0.14	1938.7	1937.82	1937.82	0.0551	27	2141.30–2315.30
Dissolved Oxygen (DO)	WQP-DO-01	Rainy	0.11	3.57	3.48	−3.48	0.0675	30	3.276–6.381
		Dry	0.02	2.73	2.53	−2.53	0.4908	27	4.819–6.074
	WQP-DO-02	Rainy	0.00	126.33	88.07	−0.11	0.7774	29	−187.58–393.29
		Dry	0.00	136.53	94.68	−65.06	0.8415	27	−408.11–140.38
	WQP-DO-03	Rainy	0.00	0.95	0.78	0.65	0.9740	30	7.680–8.754
		Dry	0.08	1.21	1.03	0.3	0.1586	27	7.468–8.815
	WQP-DO-04	Rainy	0.07	0.68	0.56	−0.15	0.16509	30	7.411–7.703
		Dry	0.00	1.12	0.94	−0.45	0.75347	27	7.268–7.608
Total Nitrogen (TN)	WQP-TN-01	Rainy	0.00	0.41	0.39	0.39	0.7668	27	0.955–1.184
		Dry	0.00	0.57	0.53	0.53	0.9506	27	0.964–1.034
	WQP-TN-02	Rainy	0.03	1.98	1.97	1.97	0.3662	27	2.649–2.727
		Dry	0.19	2.23	2.22	2.22	0.0243	27	2.677–2.715
	WQP-TN-03	Rainy	0.02	0.27	0.21	0.17	0.4560	27	0.337–1.159
		Dry	0.00	0.27	0.19	0.06	0.7288	27	0.220–0.809
	WQP-TN-04	Rainy	0.02	2.64	2.64	−2.64	0.4564	27	−1.939–−1.928
		Dry	0.31	2.41	2.4	−2.4	0.0026	27	−1.934–−1.930
	WQP-TN-05	Rainy	0.14	19.67	19.66	19.66	0.05671	27	19.245–21.471
		Dry	0.17	19.61	19.61	19.61	0.035	27	19.708–20.675
Nitrates (N)	WQP-N-01	Rainy	0.01	1.99	1.99	−1.99	0.7125	18	0.675–2.458
		Dry	0.23	2.00	1.99	−1.99	0.0841	14	1.445–1.893
	WQP-N-02	Rainy	0.01	66.62	66.62	−66.62	0.7520	18	−42.226–−1.959
		Dry	0.24	66.62	66.62	−66.62	0.0773	14	−25.314–−16.030
Ammoniacal Nitrogen (NH_3–N)	WQP-AN-01	Rainy	0.62	0.36	0.24	0.24	0.0000	21	0.161–0.994
		Dry	0.34	0.63	0.63	0.63	0.0142	17	0.616–0.797
	WQP-AN-02	Rainy	0.66	0.62	0.62	0.62	0.0000	21	0.757–0.795
		Dry	0.05	0.69	0.69	0.69	0.3876	17	0.755–0.790
	WQP-AN-03	Rainy	0.53	0.51	0.5	0.5	0.0002	21	0.578–0.847
		Dry	0.03	0.68	0.68	0.68	0.5125	17	0.714–0.811
	WQP-AN-04	Rainy	0.00	9.63×10^{70}	2.1×10^{70}	2.10×10^{70}	0.92161	21	$0.000–4.41 \times 10^{53}$
		Dry	0.08	0.09	0.08	−0.08	0.27667	17	0.000–0.000

Table A1. *Cont.*

Variable	Code	Season	R^2	RMSE	MAE	Bias	*p*-Value	n	Observed Range
Chemical Oxygen Demand (COD)	WQP-COD-01	Rainy	0.01	66.62	66.62	−66.62	0.7520	18	−66.439–−66.438
		Dry	0.24	66.62	66.62	−66.62	0.0773	14	−66.438–−66.437
Sodium (Na^+)	WQP-NA-01	Rainy	0.06	5.18	5.16	−5.16	0.21114	30	0.685–0.892
		Dry	0.00	6.06	6	−6	0.87244	27	0.555–0.838
	WQP-NA-02	Rainy	0.04	72.13	72.13	72.13	0.28142	30	78.081–78.082
		Dry	0.00	71.37	71.36	71.36	0.78992	27	78.080–78.081
Total Magnesium (Mg^{2+})	WQP-MG-01	Rainy	0.19	39.7	39.69	39.69	0.0166	30	48.891–48.892
		Dry	0.02	39.15	39.13	39.13	0.53511	27	48.891–48.892
Chlorides (Cl^-)	WQP-CL-01	Rainy	0.23	131.25	131.25	131.25	0.1923	9	135.572–135.573
		Dry	0.06	130.21	130.21	130.21	0.44402	12	135.571–135.572

Note: Chlorophyll-a was excluded from the statistical comparison as all recorded values fell below the laboratory method's limit of quantification (LOQ). Similarly, total phosphorus had only nine values above the LOQ, and suspended solids (SST) had only one value exceeding this threshold. Due to the limited quantifiable observations, these parameters are presented for reference rather than statistical validation.

Appendix B

Table A2. Performance evaluation of regression equations based on selected spectral band combinations for estimating water quality parameters during the dry season.

WQP	Bands	Model Equation	Regression			Testing		
			R^2	MAE	RMSE	R^2	MAE	RMSE
pH	B8, B9	5.2702 + 92.8338(B8) − 60.7384(B9)	0.4394	0.1235	0.1434	0.6371	0.4402	0.4822
	B1, B9	6.2567 + 70.0864(B1) − 50.9987(B9)	0.6971	0.0891	0.1054	0.1037	0.9021	0.9162
	(B1/B9) + B8A	0.0301 + 7.4127x	0.6072	0.0992	0.1200	0.1606	0.9470	0.9585
DO	(B9/B1) + B4	48.5445 − 38.9215x	0.3869	0.6626	0.7944	0.0154	3.7792	3.8135
Total Nitrogen	B2+B5	$-3316.2672 + 45318.9712x - 206214.4973x^2 + 312485.2983x^3$	0.4202	0.1165	0.1583	0.3570	1.0950	1.2134
NH_3–N	(B4/B1) + B9	$34.9331 - 62.8271x + 28.2871x^2$	0.5701	0.0200	0.0277	0.0303	0.0913	0.1149
Total Magnesium	(B9/B12) + B5	36.9210 + 42.0826x	0.4743	0.6575	0.8093	0.0020	1.8531	2.0769
Chlorides	B1, B8	11.7529 + 181.1302(B1) − 252.5469(B8)	0.4474	0.2666	0.3472	0.3059	0.3131	0.3959
	B1, B9	13.2862 + 135.1023(B1) − 222.5205(B9)	0.3973	0.2809	0.3625	0.2504	0.2318	0.2802
	(B12/B5) + B9	73.9309 + −64.1618x	0.4486	0.2444	0.3468	0.0141	0.9420	1.0928
Total Calcium	B6, B11	16.0820 + 1802.3723(B6) − 1662.6064(B11)	0.3517	3.4710	4.0576	0.6495	2.5349	2.8864
	(B11/B6) + B3	281.9817 − 225.6225x	0.3725	3.3543	3.9922	0.4962	2.1176	2.6949

Table A2. *Cont.*

WQP	Bands	Model Equation	Regression			Testing		
			R^2	MAE	RMSE	R^2	MAE	RMSE
Total Potassium	(B11/B12) + B9	−14.4719 + 14.2732x	0.4498	0.1001	0.1245	0.4737	0.3265	0.3678
	B1, B7	0.0511 + 44.5267(B1) − 35.0331(B7)	0.3066	0.1077	0.1398	0.6303	0.0539	0.0629
Total Silicon	B11, B12	−8.1044 + 324.5570(B11) − 226.0222(B12)	0.6024	0.1945	0.2422	0.4810	0.2782	0.3452
	(B11/B12) + B9	−190620.8543 + 518258.7287x −469687.3945x^2 + 141893.3150x^3	0.512	0.2123	0.2683	0.8110	0.1970	0.2522
	(B11/B12) + B1	−31.1209 + 29.8852x	0.4854	0.2167	0.2756	0.8551	0.2861	0.3636
TDS_1	B6, B11	−6.5662 + 1853.8103(B6) −1301.6422(B11)	0.5838	2.4971	3.1457	0.7341	5.7563	5.9936
	(B6/B11) + B12	−201.7290 + 227.9766x	0.5634	2.5274	3.2218	0.7115	4.6210	4.8962
	(B6/B11) + B9	−182.3844 + 210.7001x	0.5593	2.5298	3.2370	0.7388	4.9822	5.2155
TDS_2	B5, B12	4.3813 + 3887.1081(B5) −3471.2789(B12)	0.5802	1.6951	2.2519	0.6765	3.9838	4.9751
TDS_3	B6, B11	−1.8525 + 1900.1408(B6) + −1461.5655(B11)	0.5257	2.7525	3.4197	0.6967	4.7869	5.0527
	(B6/B11) + B8A	−1139.0172 + 1898.5706x + −750.0057x^2	0.5191	2.6584	3.4435	0.7201	4.1177	4.3950
	(B6/B11) + B12	223.6711x − 203.8210	0.5230	2.6916	3.4295	0.6720	3.9327	4.2565
TDS_4	(B6/B11) + B12	−200.0019 + 225.1125x	0.5583	2.5156	3.2143	0.6982	4.3385	4.6404
Salt	B6, B11	2.5467 + 1829.3356(B6) − 1399.4181(B11)	0.5532	2.4427	3.1262	0.6960	5.3591	5.5973
	(B6/B11) + B12	−191.4588 + 215.6541x	0.5479	2.4506	3.1447	0.6782	4.5235	4.7984
Metals	B6, B8A	−0.1679 −16.6738(B6) + 21.3993(B8A)	0.3783	0.0246	0.0325	0.3290	0.0289	0.0332

Table A3. Performance evaluation of regression equations based on selected spectral band combinations for estimating water quality parameters during the rainy season.

WQP	Bands	Model Equation	Regression			Testing		
			R^2	MAE	RMSE	R^2	MAE	RMSE
EC	(B1/B9) + B3	377.7439 − 94.1387x	0.8774	2.3152	3.2068	0.9118	3.8439	4.0387
	B3, B9	398.9889 −2318.2098B3 + 1266.8358B9	0.8393	2.7829	3.6705	0.9718	2.6275	2.8113
NH_3–N	(B2/B3) + B1	1.4346 − 1.2305x	0.8407	0.0155	0.0186	0.3549	0.0312	0.0360
	B2, B4	0.2373 − 13.3072B2 + 12.4165B4	0.8126	0.0166	0.0201	0.3260	0.0383	0.0485
Total Calcium	(B5/B9) + B1	−86422.9362 + 230676.0153x −204876.6823x^2 + 60573.6592x^3	0.8403	1.6281	2.1001	0.9234	2.1563	2.3505
	B3, B9	78.3624 − 1954.5532B3 + 1715.1469B9	0.7964	1.8403	2.3711	0.6416	2.9664	3.7923
	B1, B9	−54.7534 − 1001.3258B1 + 1927.8490B9	0.7779	1.9479	2.4768	0.9575	1.3660	1.6747

Table A3. *Cont.*

WQP	Bands	Model Equation	Regression			Testing		
			R^2	MAE	RMSE	R^2	MAE	RMSE
Total Copper	(B11/B1) + B9	$-0.0505 + 0.1479x - 0.1413x^2 + 0.0454x^3$	0.8738	0.0002	0.0002	0.9483	0.0002	0.0002
Total Lithium	(B8/B9) + B3	$0.0961 - 0.0783x$	0.4492	0.0009	0.0013	0.7108	0.0007	0.0010
Total Potassium	(B3/B8A) + B9	$8.3920 - 6.2236x$	0.4823	0.1067	0.1452	0.8126	0.1082	0.1242
	B3, B5	$2.5766 - 61.4031B3 + 50.7426B5$	0.4722	0.1031	0.1466	0.8222	0.0883	0.1002
Total Silicon	(B12/B3) + B9	$-15.4473 + 17.4132x$	0.7609	0.1935	0.2511	0.9141	0.2064	0.2739
Total Iron	(B7/B5) + B12	$-1.5667 + 1.4464x$	0.7020	0.0082	0.0096	*	*	*
Total Molybdenum	(B5/B9) + B1	$0.0087 - 0.0075x$	0.8052	0.00001	0.0001	*	*	*
Salt	(B6/B9) + B1	$296.1252 - 219.7282x$	0.6901	2.3660	2.9080	0.9251	0.9844	1.1013
	B6, B9	$101.7986 - 2728.5676B6 + 2257.8518B9$	0.6527	2.4232	3.0788	0.9161	0.7957	1.0024
TDS1	B1, B9	$-55.2584 - 1000.7899B1 + 2116.1663B9$	0.7555	1.9443	2.5512	0.8034	1.6790	2.0125
TDS3	B1, B9	$-62.5268 - 1040.1592B1 + 2167.5819B9$	0.8040	1.7416	2.2861	0.8306	1.6425	1.9518
TDS4	B1, B9	$-57.1627 - 991.4322B1 + 2112.9990B9$	0.7674	1.8814	2.4564	0.8311	1.5849	1.8652

Note: * Some variables could not be tested due to concentrations falling below detection thresholds.

References

1. Boyd, C.E. Physical Properties of Water. In *Water Quality: An Introduction*; Boyd, C.E., Ed.; Springer International Publishing: Cham, Switzerland, 2020; pp. 1–19, ISBN 978-3-030-23335-8.
2. Kaplan, G.; Yalcinkaya, F.; Altıok, E.; Pietrelli, A.; Nastro, R.A.; Lovecchio, N.; Ieropoulos, I.A.; Tsipa, A. The Role of Remote Sensing in the Evolution of Water Pollution Detection and Monitoring: A Comprehensive Review. *Phys. Chem. Earth Parts A/B/C* **2024**, *136*, 103712. [CrossRef]
3. Cao, X.; Zhang, J.; Meng, H.; Lai, Y.; Xu, M. Remote Sensing Inversion of Water Quality Parameters in the Yellow River Delta. *Ecol. Indic.* **2023**, *155*, 110914. [CrossRef]
4. Feyisa, G.L.; Meilby, H.; Fensholt, R.; Proud, S.R. Automated Water Extraction Index: A New Technique for Surface Water Mapping Using Landsat Imagery. *Remote Sens. Environ.* **2014**, *140*, 23–35. [CrossRef]
5. Tian, P.; Xu, Z.; Fan, W.; Lai, H.; Liu, Y.; Yang, P.; Yang, Z. Exploring the Effects of Climate Change and Urban Policies on Lake Water Quality Using Remote Sensing and Explainable Artificial Intelligence. *J. Clean. Prod.* **2024**, *475*, 143649. [CrossRef]
6. Jaywant, S.A.; Arif, K.M. Remote Sensing Techniques for Water Quality Monitoring: A Review. *Sensors* **2024**, *24*, 8041. [CrossRef] [PubMed]
7. Fouladi Osgouei, H.; Zarghami, M.; Mosaferi, M.; Karimzadeh, S. A Novel Analysis of Critical Water Pollution in the Transboundary Aras River Using the Sentinel-2 Satellite Images and ANNs. *Int. J. Environ. Sci. Technol.* **2022**, *19*, 9011–9026. [CrossRef]
8. Chang, N.-B.; Bai, K.; Chen, C.-F. Integrating Multisensor Satellite Data Merging and Image Reconstruction in Support of Machine Learning for Better Water Quality Management. *J. Environ. Manag.* **2017**, *201*, 227–240. [CrossRef] [PubMed]
9. Schmidt, S.I.; Schröder, T.; Kutzner, R.D.; Laue, P.; Bernert, H.; Stelzer, K.; Friese, K.; Rinke, K. Evaluating Satellite-Based Water Quality Sensing of Inland Waters on Basis of 100+ German Water Bodies Using 2 Different Processing Chains. *Remote Sens.* **2024**, *16*, 3416. [CrossRef]

10. Lehmann, M.K.; Gurlin, D.; Pahlevan, N.; Alikas, K.; Conroy, T.; Anstee, J.; Balasubramanian, S.V.; Barbosa, C.C.F.; Binding, C.; Bracher, A.; et al. GLORIA—A Globally Representative Hyperspectral in Situ Dataset for Optical Sensing of Water Quality. *Sci Data* **2023**, *10*, 100. [CrossRef] [PubMed]
11. Ali, A.; Zhou, G.; Pablo Antezana Lopez, F.; Xu, C.; Jing, G.; Tan, Y. Deep Learning for Water Quality Multivariate Assessment in Inland Water across China. *Int. J. Appl. Earth Obs. Geoinf.* **2024**, *133*, 104078. [CrossRef]
12. Zhao, Y.; He, X.; Pan, S.; Bai, Y.; Wang, D.; Li, T.; Gong, F.; Zhang, X. Satellite Retrievals of Water Quality for Diverse Inland Waters from Sentinel-2 Images: An Example from Zhejiang Province, China. *Int. J. Appl. Earth Obs. Geoinf.* **2024**, *132*, 104048. [CrossRef]
13. Arias-Rodriguez, L.F.; Duan, Z.; Díaz-Torres, J.d.J.; Basilio Hazas, M.; Huang, J.; Kumar, B.U.; Tuo, Y.; Disse, M. Integration of Remote Sensing and Mexican Water Quality Monitoring System Using an Extreme Learning Machine. *Sensors* **2021**, *21*, 4118. [CrossRef] [PubMed]
14. Observatorio Nacional de Recursos Hídricos. Available online: https://snirh.ana.gob.pe/onrh/ (accessed on 2 December 2024).
15. Deng, Y.; Zhang, Y.; Pan, D.; Yang, S.X.; Gharabaghi, B. Review of Recent Advances in Remote Sensing and Machine Learning Methods for Lake Water Quality Management. *Remote Sens.* **2024**, *16*, 4196. [CrossRef]
16. INRENA Plan Maestro de La Reserva Nacional de Junín, 2008–2012. Available online: https://sis.sernanp.gob.pe/biblioteca/?publicacion=1802 (accessed on 1 November 2024).
17. Pérez, L.F.C.; Zambrano, G.A.M. Contaminación por aguas residuales e indicadores de calidad en la reserva nacional 'Lago Junín', Perú. *Rev. Mex. Cienc. Agrícolas* **2019**, *10*, 1433–1447. [CrossRef]
18. Castillo, L.; Elias, R. Descripción En Época Seca Del Microhábitat Del Renacuajo de Telmatobius Macrostomus (Peters, 1873) "Rana Gigante Del Lago Junín" En Los Afluentes Del Lago Chinchaycocha/Perú. *Ecol. Apl.* **2021**, *20*, 25–34. [CrossRef]
19. Autoridad Nacional del Agua. *Monitoreo Participativo de la Calidad de los Recursos Hídricos en la Cuenca Mantaro (2019-IV)*; Autoridad Nacional Del Agua: Lima, Peru, 2020.
20. Autoridad Nacional del Agua. *Quinto Monitoreo de la Calidad de Agua Superficial Dle Lago Chinchaycocha-Epoca de Estiaje*; Autoridad Nacional del Agua: Lima, Peru, 2018.
21. MINAM Resolución Suprema N° 005-2017-MINAM. Available online: https://www.minam.gob.pe/disposiciones/resolucion-suprema-n-005-2017-minam/ (accessed on 1 November 2024).
22. Yanqui, R.M.; Minaya, L.C.; Balbín, M.V. Almacenamiento de carbono en especies predominantes de flora en el lago Chinchaycocha. *Apunt. Cienc. Soc.* **2012**, *2*, 6. [CrossRef]
23. SERFOR Libro Rojo de La Fauna Silvestre Amenazada Del Perú | SINIA. Available online: https://sinia.minam.gob.pe/documentos/libro-rojo-fauna-silvestre-amenazada-peru (accessed on 1 November 2024).
24. Tejada Moncada, A. *Evaluación e Identificación de Potenciales Riesgos Ambientales en Flora y Fauna en Laguna Chinchaycocha, Junín, Departamento de Junín*; Organismo de Evaluación y Fiscalización Ambiental (OEFA): Lima, Peru, 2013.
25. Gonzales Rossel, J.A.; Olivares Alcántara, V.M. *Informe de Resultados de la Evaluación Ambiental Realizado en los Ámbitos de la Actividad Minera en las Cuencas de los ríos San Juan y San José en el Departamento de Cerro de Pasco*; Organismo de Evaluación y Fiscalización Ambiental–OEFA: Lima, Peru, 2012.
26. Ministerio del Ambiente Mapa Nacional de Cobertura Vegetal. Available online: https://geoservidor.minam.gob.pe/ (accessed on 22 February 2025).
27. Ministerio de Desarrollo Agrario y Riego Atlas de la Superficie Agrícola del Perú. Available online: https://siea.midagri.gob.pe/portal/informativos/superficie-agricola-peruana (accessed on 22 February 2025).
28. GEO ANP. Available online: https://geo.sernanp.gob.pe/visorsernanp/ (accessed on 4 May 2025).
29. Ministerio de Energía y Minas. *Resolución Ministerial N.° 056-2025-MINEM/DM. Actualización del Inventario Inicial de Pasivos Ambientales Mineros*; Ministerio de Energía y Minas: Santo Domingo, Dominican Republic, 2025.
30. Kayastha, P.; Dzialowski, A.R.; Stoodley, S.H.; Wagner, K.L.; Mansaray, A.S. Effect of Time Window on Satellite and Ground-Based Data for Estimating Chlorophyll-a in Reservoirs. *Remote Sens.* **2022**, *14*, 846. [CrossRef]
31. Zhai, M.; Zhou, X.; Tao, Z.; Xie, Y.; Yang, J.; Shao, W.; Zhang, H.; Lv, T. Satellite-Ground Synchronous in-Situ Dataset of Water Optical Parameters and Surface Temperature for Typical Lakes in China. *Sci. Data* **2024**, *11*, 883. [CrossRef] [PubMed]
32. Yang, J.; Deng, R.; Ma, Y.; Li, J.; Guo, Y.; Lei, C. Satellite Retrieval and Spatiotemporal Variability in Chlorophyll-a for Marine Ranching: An Example from Daya Bay, Guangdong Province, China. *Water* **2025**, *17*, 780. [CrossRef]
33. Park, J.; Khanal, S.; Zhao, K.; Byun, K. Remote Sensing of Chlorophyll-a and Water Quality over Inland Lakes: How to Alleviate Geo-Location Error and Temporal Discrepancy in Model Training. *Remote Sens.* **2024**, *16*, 2761. [CrossRef]
34. Hestir, E.L.; Brando, V.E.; Bresciani, M.; Giardino, C.; Matta, E.; Villa, P.; Dekker, A.G. Measuring Freshwater Aquatic Ecosystems: The Need for a Hyperspectral Global Mapping Satellite Mission. *Remote Sens. Environ.* **2015**, *167*, 181–195. [CrossRef]
35. Aprueban Estándares de Calidad Ambiental (ECA) Para Agua y Establecen Disposiciones Complementarias | SINIA. Available online: https://sinia.minam.gob.pe/normas/aprueban-estandares-calidad-ambiental-eca-agua-establecen-disposiciones (accessed on 2 December 2024).
36. European Space Agency. *Sentinel-2 User Handbook*; European Space Agency: Paris, France, 2015.

37. Torres-Bejarano, F.; Arteaga-Hernández, F.; Rodríguez-Ibarra, D.; Mejía-Ávila, D.; González-Márquez, L.C. Water Quality Assessment in a Wetland Complex Using Sentinel 2 Satellite Images. *Int. J. Environ. Sci. Technol.* **2021**, *18*, 2345–2356. [CrossRef]
38. Pizani, F.M.C.; Maillard, P.; Ferreira, A.F.F.; de Amorim, C.C. Estimation of water quality in a reservoir from sentinel-2 msi and landsat-8 oli sensors. *ISPRS Ann. Photogramm. Remote Sens. Spat. Inf. Sci.* **2020**, *V-3-2020*, 401–408. [CrossRef]
39. Ndou, N. Geostatistical Inference of Sentinel-2 Spectral Reflectance Patterns to Water Quality Indicators in the Setumo Dam, South Africa. *Remote Sens. Appl. Soc. Environ.* **2023**, *30*, 100945. [CrossRef]
40. Lesa Chundu, M.; Banda, K.; Sichingabula, H.M.; Nyambe, I.A. Integrated Water Quality Assessment of Open Water Bodies Using Empirical Equations and Remote Sensing Techniques in Bangweulu Wetland Lakes, Zambia. *J. Gt. Lakes Res.* **2024**, 102451. [CrossRef]
41. El Ouali, A.; El Hafyani, M.; Roubil, A.; Lahrach, A.; Essahlaoui, A.; Hamid, F.E.; Muzirafuti, A.; Paraforos, D.S.; Lanza, S.; Randazzo, G. Modeling and Spatiotemporal Mapping of Water Quality through Remote Sensing Techniques: A Case Study of the Hassan Addakhil Dam. *Appl. Sci.* **2021**, *11*, 9297. [CrossRef]
42. Hossen, H.; Mahmod, W.E.; Negm, A.; Nakamura, T. Assessing Water Quality Parameters in Burullus Lake Using Sentinel-2 Satellite Images. *Water Resour.* **2022**, *49*, 321–331. [CrossRef]
43. Kowe, P.; Ncube, E.; Magidi, J.; Ndambuki, J.M.; Rwasoka, D.T.; Gumindoga, W.; Maviza, A.; de jesus Paulo Mavaringana, M.; Kakanda, E.T. Spatial-Temporal Variability Analysis of Water Quality Using Remote Sensing Data: A Case Study of Lake Manyame. *Sci. Afr.* **2023**, *21*, e01877. [CrossRef]
44. Ouma, Y.O.; Noor, K.; Herbert, K. Modelling Reservoir Chlorophyll-a, TSS, and Turbidity Using Sentinel-2A MSI and Landsat-8 OLI Satellite Sensors with Empirical Multivariate Regression. *J. Sens.* **2020**, *2020*, 8858408. [CrossRef]
45. Wang, Y.; Xia, H.; Fu, J.; Sheng, G. Water Quality Change in Reservoirs of Shenzhen, China: Detection Using LANDSAT/TM Data. *Sci. Total Environ.* **2004**, *328*, 195–206. [CrossRef] [PubMed]
46. Muhoyi, H.; Gumindoga, W.; Mhizha, A.; Misi, S.N.; Nondo, N. Water Quality Monitoring Using Remote Sensing, Lower Manyame Sub-Catchment, Zimbabwe. *Water Pract. Technol.* **2022**, *17*, 1347–1357. [CrossRef]
47. Torbick, N.; Hession, S.; Hagen, S.; Wiangwang, N.; Becker, B.; Qi, J. Mapping Inland Lake Water Quality across the Lower Peninsula of Michigan Using Landsat TM Imagery. *Int. J. Remote Sens.* **2013**, *34*, 7607–7624. [CrossRef]
48. Kapalanga, T.S.; Hoko, Z.; Gumindoga, W.; Chikwiramakomo, L. Remote-Sensing-Based Algorithms for Water Quality Monitoring in Olushandja Dam, North-Central Namibia. *Water Supply* **2020**, *21*, 1878–1894. [CrossRef]
49. Dong, G.; Hu, Z.; Liu, X.; Fu, Y.; Zhang, W. Spatio-Temporal Variation of Total Nitrogen and Ammonia Nitrogen in the Water Source of the Middle Route of the South-To-North Water Diversion Project. *Water* **2020**, *12*, 2615. [CrossRef]
50. Liu, T.; Guo, Z.; Li, X.; Xiao, T.; Liu, J.; Zhang, Y. Monitoring Water Quality Parameters Using Sentinel-2 Data: A Case Study in the Weihe River Basin (China). *Sustainability* **2024**, *16*, 6881. [CrossRef]
51. Shi, X.; Qiu, Z.; Hu, Y.; Zhao, D.; Zhao, A.; Lin, H.; Zhan, Y.; Wang, Y.; Zhang, Y. Monitoring the Water Quality Distribution Characteristics in the Huaihe River Basin Based on the Sentinel-2 Satellite. *Water* **2024**, *16*, 860. [CrossRef]
52. Ismail, K.; Boudhar, A.; Abdelkrim, A.; Mohammed, H.; Mouatassime, S.E.; Kamal, A.O.; Driss, E.; Idrissi, E.A.; Nouaim, W. Evaluating the Potential of Sentinel-2 Satellite Images for Water Quality Characterization of Artificial Reservoirs: The Bin El Ouidane Reservoir Case Study (Morocco). *Meteorol. Hydrol. Water Manag.* **2019**, *7*, 31–39. [CrossRef]
53. Song, C.; Huang, B.; Ke, L.; Richards, K.S. Remote Sensing of Alpine Lake Water Environment Changes on the Tibetan Plateau and Surroundings: A Review. *ISPRS J. Photogramm. Remote Sens.* **2014**, *92*, 26–37. [CrossRef]
54. Maslukah, L.; Basayep, I.; Wirasatriya, A.; Indrayanti, E.; Prasetyawan, I.B.; Wijaya, Y.J. Application of Sentinel-2 Imagery for Total Suspended Solids Mapping off the Bodri River, Kendal Regency, Indonesia. *Remote Sens. Appl. Soc. Environ.* **2024**, *36*, 101379. [CrossRef]
55. Wirasatriya, A.; Maslukah, L.; Indrayanti, E.; Yusuf, M.; Milenia, A.P.; Adam, A.A.; Helmi, M. Seasonal Variability of Total Suspended Sediment off the Banjir Kanal Barat River, Semarang, Indonesia Estimated from Sentinel-2 Images. *Reg. Stud. Mar. Sci.* **2023**, *57*, 102735. [CrossRef]
56. Abdelmalik, K.W. Role of Statistical Remote Sensing for Inland Water Quality Parameters Prediction. *Egypt. J. Remote Sens. Space Sci.* **2018**, *21*, 193–200. [CrossRef]
57. Jiang, J.; Chen, Z.; Sun, K.; Chen, Y.; Mu, M.; Sun, Q.; Zeng, S. Monitoring 36-Year Water Clarity Dynamics in Turbid Waters of the Pearl River Estuary, China, Using Landsat Data. *Ecol. Inform.* **2024**, *81*, 102600. [CrossRef]
58. Briceño-de-Urbaneja, I.; Pérez, W.; Miguel, D.S.; Ramos, S. Determinación de calidad de agua en el Lago Vichuquén, con imágenes de satélite Landsat 8, sensor OLI, año 2016, Chile. *Rev. De Teledetección* **2018**, 67–78. [CrossRef]
59. Jang, W.; Kim, J.; Kim, J.H.; Shin, J.-K.; Chon, K.; Kang, E.T.; Park, Y.; Kim, S. Evaluation of Sentinel-2 Based Chlorophyll-a Estimation in a Small-Scale Reservoir: Assessing Accuracy and Availability. *Remote Sens.* **2024**, *16*, 315. [CrossRef]
60. Saberioon, M.; Brom, J.; Nedbal, V.; Souček, P.; Císař, P. Chlorophyll-a and Total Suspended Solids Retrieval and Mapping Using Sentinel-2A and Machine Learning for Inland Waters. *Ecol. Indic.* **2020**, *113*, 106236. [CrossRef]

61. Gerardo, R.; de Lima, I.P. Monitoring Duckweeds (Lemna Minor) in Small Rivers Using Sentinel-2 Satellite Imagery: Application of Vegetation and Water Indices to the Lis River (Portugal). *Water* **2022**, *14*, 2284. [CrossRef]
62. Xu, H. Modification of Normalised Difference Water Index (NDWI) to Enhance Open Water Features in Remotely Sensed Imagery. *Int. J. Remote Sens.* **2006**, *27*, 3025–3033. [CrossRef]
63. Khan, N.M.; Rastoskuev, V.V.; Sato, Y.; Shiozawa, S. Assessment of Hydrosaline Land Degradation by Using a Simple Approach of Remote Sensing Indicators. *Agric. Water Manag.* **2005**, *77*, 96–109. [CrossRef]
64. Guo, H.; Wang, X.; Ouyang, Z.; Chen, S.; Che, T.; Zheng, Z. Application of the ESTARFM Algorithm for Fusing Sentinel-2 and MODIS NDSI Series in the Eastern Qilian Mountains. *J. Hydrol. Reg. Stud.* **2025**, *57*, 102103. [CrossRef]
65. Villa, P.; Laini, A.; Bresciani, M.; Bolpagni, R. A Remote Sensing Approach to Monitor the Conservation Status of Lacustrine Phragmites Australis Beds. *Wetl. Ecol. Manag.* **2013**, *21*, 399–416. [CrossRef]
66. Tucker, C.J. Red and Photographic Infrared Linear Combinations for Monitoring Vegetation. *Remote Sens. Environ.* **1979**, *8*, 127–150. [CrossRef]
67. Gitelson, A.A.; Merzlyak, M.N. Signature Analysis of Leaf Reflectance Spectra: Algorithm Development for Remote Sensing of Chlorophyll. *J. Plant Physiol.* **1996**, *148*, 494–500. [CrossRef]
68. Lacaux, J.P.; Tourre, Y.M.; Vignolles, C.; Ndione, J.A.; Lafaye, M. Classification of Ponds from High-Spatial Resolution Remote Sensing: Application to Rift Valley Fever Epidemics in Senegal. *Remote Sens. Environ.* **2007**, *106*, 66–74. [CrossRef]
69. Mukherjee, N.R.; Samuel, C. Assessment of the Temporal Variations of Surface Water Bodies in and around Chennai Using Landsat Imagery. *Indian J. Sci. Technol.* **2016**, *9*, 1–7. [CrossRef]
70. Zeng, S.; Lei, S.; Qin, Z.; Song, W.; Sun, Q. Long-Term Remote Observations of Particulate Organic Phosphorus Concentration in Eutrophic Lake Taihu Based on a Novel Algorithm. *Chemosphere* **2023**, *332*, 138836. [CrossRef] [PubMed]
71. Ayala Izurieta, J.E.; Beltrán Dávalos, A.A.; Jara Santillán, C.A.; Godoy Ponce, S.C.; Van Wittenberghe, S.; Verrelst, J.; Delegido, J. Spatial and Temporal Analysis of Water Quality in High Andean Lakes with Sentinel-2 Satellite Automatic Water Products. *Sensors* **2023**, *23*, 8774. [CrossRef] [PubMed]
72. Shrivastava, P.; Kumar, R. Soil Salinity: A Serious Environmental Issue and Plant Growth Promoting Bacteria as One of the Tools for Its Alleviation. *Saudi J. Biol. Sci.* **2015**, *22*, 123–131. [CrossRef] [PubMed]
73. Sunardi, S.; Ariyani, M.; Agustian, M.; Withaningsih, S.; Parikesit, P.; Juahir, H.; Ismail, A.; Abdoellah, O.S. Water Corrosivity of Polluted Reservoir and Hydropower Sustainability. *Sci. Rep.* **2020**, *10*, 11110. [CrossRef] [PubMed]
74. Arias-Rodriguez, L.F.; Tüzün, U.F.; Duan, Z.; Huang, J.; Tuo, Y.; Disse, M. Global Water Quality of Inland Waters with Harmonized Landsat-8 and Sentinel-2 Using Cloud-Computed Machine Learning. *Remote Sens.* **2023**, *15*, 1390. [CrossRef]
75. Rodríguez-López, L.; Bravo Alvarez, L.; Duran-Llacer, I.; Ruíz-Guirola, D.E.; Montejo-Sánchez, S.; Martínez-Retureta, R.; López-Morales, E.; Bourrel, L.; Frappart, F.; Urrutia, R. Leveraging Machine Learning and Remote Sensing for Water Quality Analysis in Lake Ranco, Southern Chile. *Remote Sens.* **2024**, *16*, 3401. [CrossRef]
76. Lins, R.C.; Martinez, J.-M.; Motta Marques, D.D.; Cirilo, J.A.; Fragoso, C.R. Assessment of Chlorophyll-a Remote Sensing Algorithms in a Productive Tropical Estuarine-Lagoon System. *Remote Sens.* **2017**, *9*, 516. [CrossRef]
77. Fendereski, F.; Creed, I.F.; Trick, C.G. Remote Sensing of Chlorophyll-a in Clear vs. Turbid Waters in Lakes. *Remote Sens.* **2024**, *16*, 3553. [CrossRef]
78. Espinoza, J.C.; Chavez, S.; Ronchail, J.; Junquas, C.; Takahashi, K.; Lavado, W. Rainfall Hotspots over the Southern Tropical Andes: Spatial Distribution, Rainfall Intensity, and Relations with Large-Scale Atmospheric Circulation. *Water Resour. Res.* **2015**, *51*, 3459–3475. [CrossRef]
79. Coelho, C.; Heim, B.; Foerster, S.; Brosinsky, A.; De Araújo, J.C. In Situ and Satellite Observation of CDOM and Chlorophyll-a Dynamics in Small Water Surface Reservoirs in the Brazilian Semiarid Region. *Water* **2017**, *9*, 913. [CrossRef]
80. Brewin, R.J.W.; Ciavatta, S.; Sathyendranath, S.; Skákala, J.; Bruggeman, J.; Ford, D.; Platt, T. The Influence of Temperature and Community Structure on Light Absorption by Phytoplankton in the North Atlantic. *Sensors* **2019**, *19*, 4182. [CrossRef] [PubMed]
81. Peralta-Guevara, D.E.; Quispe-Quispe, Y.; Palomino-Malpartida, Y.G.; Aronés-Medina, E.G.; Correa-Cuba, O.; Aróstegui León, E.; Carhuarupay-Molleda, Y.F.; Alzamora-Flores, H.; Licapa Redolfo, R.; Pumallihua Ramos, M.; et al. A High Andean Lake: A Current Look at Anthropogenic Activities and Water Quality. *Water* **2025**, *17*, 1182. [CrossRef]
82. Alcântara, E.; Bernardo, N.; Watanabe, F.; Rodrigues, T.; Rotta, L.; Carmo, A.; Shimabukuro, M.; Gonçalves, S.; Imai, N. Estimating the CDOM Absorption Coefficient in Tropical Inland Waters Using OLI/Landsat-8 Images. *Remote Sens. Lett.* **2016**, *7*, 661–670. [CrossRef]
83. Ramírez-Suárez, W.M.; Hernández-Olivera, L.A. Tolerancia a La Salinidad En Especies Cespitosas. *Pastos Forrajes* **2016**, *39*, 235–245.
84. García Aragón, F.; Ysla Cedeño, E.A.; Bazán Alguiar, J.P.; Saldaña Alfaro, D.R.; Llanos Vásquez, C.F. *Informe de Evaluación Ambiental del Lago Chinchaycocha, Ejecutado Durante el año 2015*; Organismo de Evaluación y Fiscalización Ambiental–Oefa: Lima, Peru, 2015.

85. Castro-González, M.; Campos, N.H. Efecto del Cadmio y el Cobre sobre el Flujo de Nitrógeno y Fósforo en la Interfase Agua-Sedimento en una Laguna Costera Tropical. *Rev. Acad. Colomb. Cienc. Exactas Físicas Nat.* **2004**, *28*, 535–543. [CrossRef]
86. Xu, X.; Pan, J.; Zhang, H.; Lin, H. Progress in Remote Sensing of Heavy Metals in Water. *Remote Sens.* **2024**, *16*, 3888. [CrossRef]
87. Adjovu, G.E.; Stephen, H.; James, D.; Ahmad, S. Measurement of Total Dissolved Solids and Total Suspended Solids in Water Systems: A Review of the Issues, Conventional, and Remote Sensing Techniques. *Remote Sens.* **2023**, *15*, 3534. [CrossRef]
88. Ngamile, S.; Madonsela, S.; Kganyago, M. Trends in Remote Sensing of Water Quality Parameters in Inland Water Bodies: A Systematic Review. *Front. Environ. Sci.* **2025**, *13*, 1549301. [CrossRef]
89. Batina, A.; Krtalić, A. Integrating Remote Sensing Methods for Monitoring Lake Water Quality: A Comprehensive Review. *Hydrology* **2024**, *11*, 92. [CrossRef]
90. Felegari, S.; Sharifi, A.; Khosravi, M.; Sabanov, S.; Tariq, A.; Karuppannan, S. Using Sentinel-2 Data to Estimate the Concentration of Heavy Metals Caused by Industrial Activities in Ust-Kamenogorsk, Northeastern Kazakhstan. *Heliyon* **2023**, *9*, e21908. [CrossRef] [PubMed]

Disclaimer/Publisher's Note: The statements, opinions and data contained in all publications are solely those of the individual author(s) and contributor(s) and not of MDPI and/or the editor(s). MDPI and/or the editor(s) disclaim responsibility for any injury to people or property resulting from any ideas, methods, instructions or products referred to in the content.